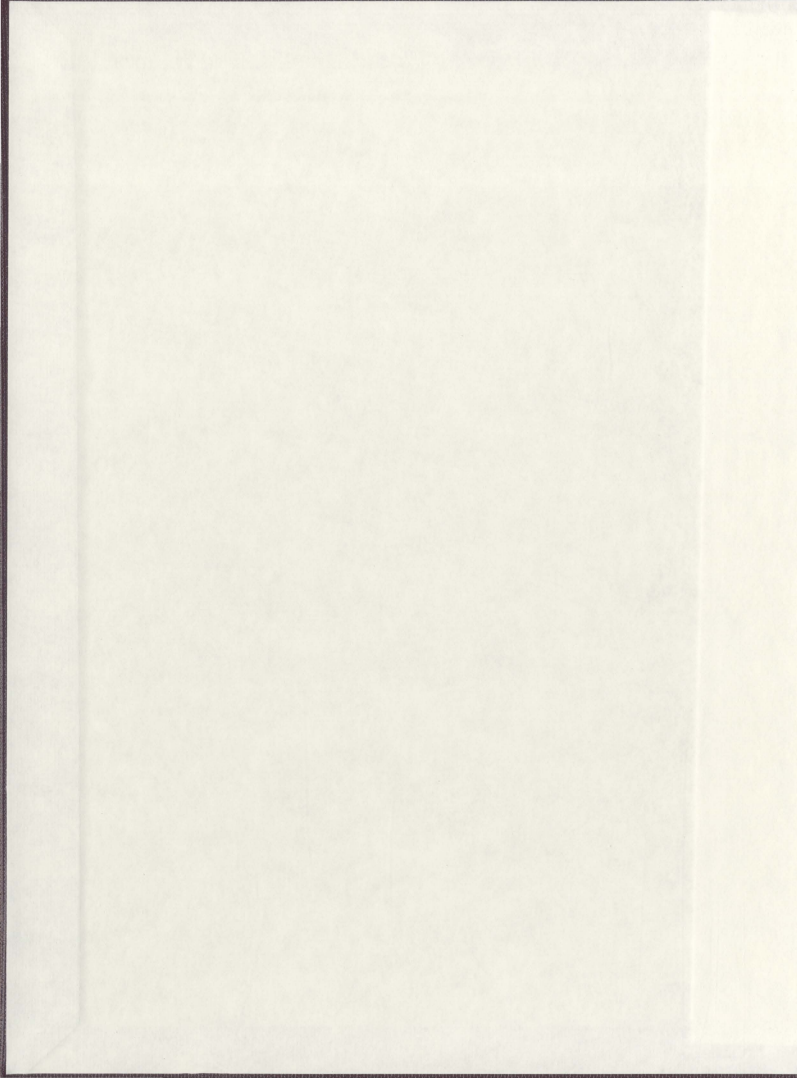# CHARACTERIZING THE TUNDRA TAIGA INTERFACE USING RADARSAT-2 (MEALY MOUNTAINS, LABRADOR)

HEATHER WARD

Characterizing the tundra taiga interface using Radarsat-2 (Mealy Mountains, Labrador).

Author: Heather Ward

Student number: 200542330

This thesis is submitted to the

School of Graduate Studies,

Memorial University of Newfoundland

in partial fulfillment of the

requirements for the degree of

Master of Science,

Department of Geography

April 2012

**Abstract**

The transition zone between the boreal forest and Arctic tundra, also known as the tundra taiga interface (TTI), is a unique and sensitive ecosystem. A convenient way to monitor and understand TTI changes is through the interpretation and analysis of earth observation satellite images, or remote sensing. Ecosystem monitoring provides useful information about vegetation distribution and global climate. Currently, vegetation is monitored at both global and regional scales through the use of multispectral, light detection and ranging and synthetic aperture radar imagery. Each remote sensing technology offers unique spatial, spectral and radiometric resolution sets.

This thesis investigates the use of synthetic aperture radar images from the Canadian Space Agency's RADARSAT-2 satellite to derive an image product discriminating different types of vegetation cover within the TTI region of Labrador.

A selection of texture measures was applied to a dataset consisting of six RADARSAT-1 and fourteen RADARSAT-2 images. Statistical parameters were utilized to measure how strongly the radar derived vegetation product correlated with the well-established normalized difference vegetation index (NDVI). The analysis was guided and validated by field data describing forest and non-forest land cover types.

The results indicate that a mean texture measure with a window size relating to a ground area of 330x330 m (fine mode) and 450x450 m (standard mode) applied to an R-2 HV-polarized image is able to inform on the location of the TTI and also complements the vegetation cover found in NDVI images.

## Acknowledgements

**Table of Contents**

# List of Tables

## List of Figures

# List of Equations

## List of Abbreviations

ALOS: Advanced Land Observation Satellite

ERS: European Remote Sensing

ETM+: Enhanced Thematic Mapper Plus

HRVIR: High Resolution Visible and Infrared (SPOT sensor)

IKONOS: Greek term for 'image'

IPY: International Polar Year

L-7: Landsat-7 or Land remote sensing Satellite-7

LHRG: Labrador Highlands Research Group

LiDAR: Light Detection and Ranging

MISR: Multi-angle Imaging SpectroRadiometer

MODIS: Moderate Resolution Imaging Spectroradiometer

NDVI: Normalized Differenced Vegetation Index

PALSAR: Phased Array type L-band Synthetic Aperture Radar

Radar: Radio Detection and Ranging

R-1: RADARSAT-1

R-2: RADARSAT -2

SAR: Synthetic Aperture Radar

SPOT: *Système Probatoire d'Observation de la Terre*

TTI: tundra taiga interface

TM: Thematic Mapper

# Chapter 1: Introduction

## 1.0 Introduction

Recent climate projections of habitat distribution suggest that vegetation within an alpine ecosystem will begin to migrate up slope, thus expanding in range (Payette *et al.*, 2001 and Guisan and Zimmermann, 2000). The factors that may contribute to this change are complex in nature and have encouraged researchers to look more closely at regions where these transformations are occurring. One such region is the tundra taiga interface (TTI), or the Arctic tree line, where the boreal forest meets with the Arctic tundra ecosystem in the northern hemisphere. The TTI is of importance because boreal forest and tundra ecosystems are vital components of Earth's climate system (Bonan *et al.*, 1995) and support a diverse scope of flora and fauna (Loehle and Leblanc, 1996). The item of interest in monitoring this transition zone is the distribution of forest extent, or movement of the tree line. This can indicate, over time, if there is a general net gain or net loss of forest vegetation.

Images gathered from the red and near infrared bands of multispectral satellite data to form a normalized difference vegetation index (NDVI) are an important source of information about the spatial and temporal dynamics of land cover at the TTI (Masek, 2001 and Liu *et al.*, 2005). There are particular downfalls, however, of multispectral image data, especially when acquiring a multi-year data set for the purposes of change detection. These downfalls include loss of data due to interference of the electromagnetic energy with atmospheric particles and the difficulty of producing radiometrically consistent representations of green biomass (Ranson *et al.*, 2004). Image data from

RADARSAT-1 (R-1), a satellite-based synthetic aperture radar (SAR), has been proven effective for the application of vegetation detection at transition ecosystems (Ranson *et al.*, 2004). RADARSAT-2 (R-2), launched in 2007, is the successor of R-1, and offers several technological enhancements, including the ability to image in all polarization modes and higher spatial resolution. These improvements are expected to allow for better discrimination of land cover types (Van der Sanden, 2004). Since R-2 is a relatively new satellite, little work has been completed on how it can be used to inform and predict the position of the Arctic tree line. There is little known about the land imaging characteristics of R-2, however, it is capable of relaying information on biomass, vegetation height and the identification of tree islands. It is beneficial to exploit new SAR technology and explore the specifications and limitations of R-2 data to the vegetation transition zone at the Arctic tree line.

## 1.1 Objectives

This project proposes the use of SAR images from the Canadian Space Agency's R-2 satellite, launched in 2007, to derive an image product representing vegetation cover within the TTI region of Labrador. The methodological objective of this project is to extract texture and backscatter information from radar imagery that represents the vegetation cover. The operational objective is to create a radar image-derived vegetation variable that correlates highly with the 'normalized difference vegetation index' (NDVI) image. This project also aims to identify the most useful R-2 image mode for characterizing information about the TTI.

## 1.2 Context

The research project is being conducted as part of the inter-disciplinary project 'Present processes, past changes, spatiotemporal dynamics Arctic' (PPSA) which is an International Polar Year initiative. The project contributes to an ongoing Canada-wide research effort in studying the effects of climate change on the position and structure of the tree line at Arctic sites around the globe. Specifically, the research conducted for this project will produce a new remote sensing method using R-2 SAR imagery for characterizing the spatio-temporal variations of land cover within the TTI ecosystem, to allow for integration with, and improvement upon, existing remote sensing methods.

The results of this thesis are useful to characterize the TTI at both a local and a global scale in order to better understand the social, cultural and environmental impacts that may result from changing ecosystems. The creation of a radar-derived vegetation variable will allow for more extensive and reliable spatio-temporal analysis of the tree line in Labrador, and the Arctic region as a whole. The derived product will be useful for quantitative and qualitative studies relating to the taiga-tundra ecosystem, including land cover change, tree stand type and structure identification, and forecast modelling. For Labrador, this will mean a greater understanding of the TTI ecosystem and the impacts of ecological changes on local hydrology, soil characteristics, climate, wildlife and people living in northern communities. The study site is located within the confines of the proposed Mealy Mountains National Park Reserve, and the results produced through this thesis will be used to gain a deeper understanding of the vegetation dynamics within the park and assist with future monitoring programmes to track Ecological Integrity of the park. In addition, this project will evaluate the discriminating capabilities of image

backscattering for R-2 and will contribute to the development of methods of analysis that utilize image texture.

Images were acquired for this project through the Canadian Space Agency's 'Science and Operational Applications Research–Education' (SOAR-E) initiative (project #5009). The objective of the SOAR-E program is 'to build on the successes of RADARSAT-1 by developing methods and information products to address the needs of the application sectors using the new capabilities of RADARSAT-2' (CSA, 2008).

## 1.3 Study Area

Labrador offers a unique landscape for tree line studies because it contains one of the last Boreal forest regions in Canada that has not been significantly affected by development projects such as forestry, agriculture and mining (Roberts *et al.*, 2006). This near pristine environment is ideal to monitor and predict natural changes within the TTI.

The study area for this project is located in the Mealy Mountains region of Labrador, Canada, about 20 km southeast of Etagaulet Bay situated along the central southeast shore of Lake Melville (Figure 1.1). The centre coordinates are 53°35"48' N, 58°55"05' W. The length and width measure approximately 8 km x 8 km. The region of interest is contained in a glacial valley in the eastern part of the study area, where the terrain elevation varies between 500 and 600 m (Figure 1.2). The study area is the main study site for the PPSA research project of Memorial University of Newfoundland. The northwest portion of the study area contains mountainous terrain with southeast orientated slopes. The terrain elevation ranges from about 430 to 1,100 m.
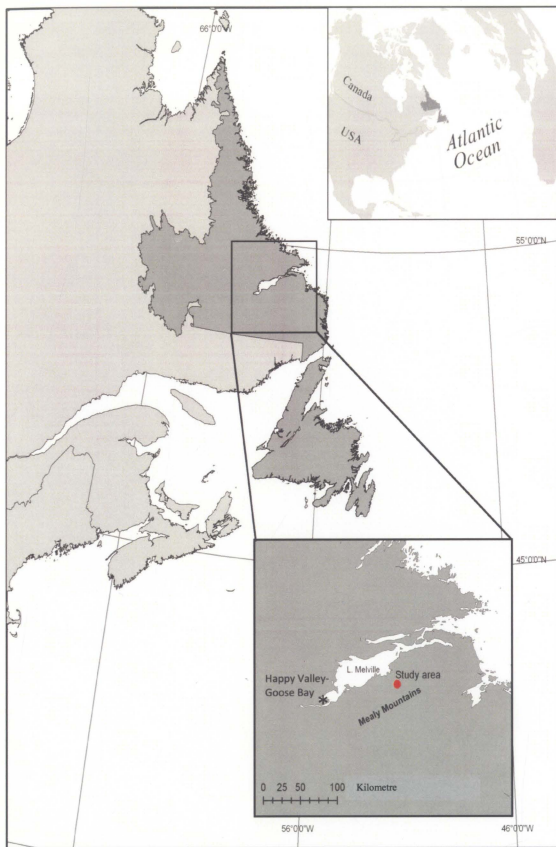
Figure 1.1: Location of the study area.
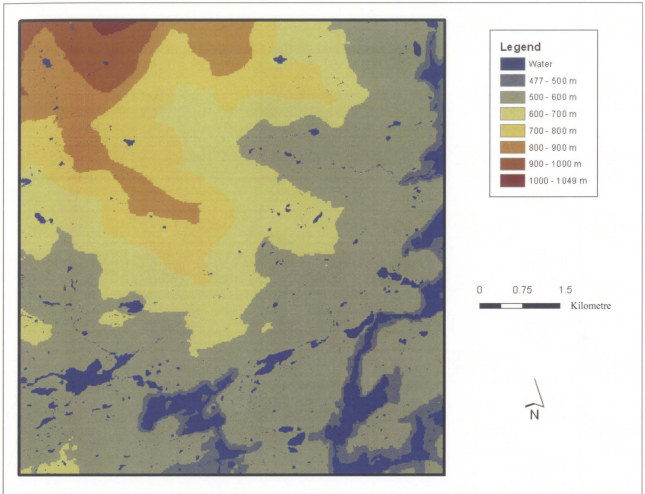
Figure 1.2: Digital elevation model of the study area. The represented area is 8 x 8 km.

## 1.4 Thesis organization

This thesis is organized into seven chapters. Subsequent to this introduction, the second chapter presents an overview of background literature related to location and structure of the tundra taiga transition zone. A particular emphasis is given to remote sensing approaches. The third chapter outlines the data needed to support the analyses and evaluation of the radar product. The fourth chapter highlights the methods that are utilized to establish the radar-derived vegetation product. The methods are presented as two separate sections, including image pre-processing, and backscatter and texture analysis. In the fifth chapter, the results are presented, divided into two main sub-sections. The first section focuses on the results obtained from the R-1 image analysis only, while the second presents the results obtained from the R-2 image data set. The two remaining sections contain a discussion of the results and a presentation of conclusions that can be drawn from this research.

# Chapter 2: Literature Review

## 2.0 Introduction

The main purpose of Earth observation remote sensing is to better understand the natural and built environments from measurements of reflected, backscattered or emitted electromagnetic (EM) energy. Remote sensing infers statistical or physical relationships between EM characteristics and a particular parameter or parameters of interest. For this research project, the parameter of interest is land cover type, or more specifically, forest and non-forest vegetation. This literature review provides a comprehensive overview of studies that encompass the integration of ecology, Arctic plant biology and different types of remote sensing methods. A special focus is given to current literature as it pertains to radar remote sensing of land cover.

This literature review comprises six major sections. The first section defines the 'tundra taiga interface' (TTI) as the term applies throughout this project. The second section investigates current remote sensing methods that are used to describe the land cover. This section includes an overview of multispectral, LiDAR and radar remote sensing methods. The third section highlights the study area's vegetation composition and structure in order to illustrate how these can be exploited during radar remote sensing analysis to better represent the land cover. The fourth section presents image analysis procedures that are used to extract land cover information, including backscatter analysis, texture analysis and geostatistical methods investigating the spatial nature of data. The concluding section illustrates the potential that radar data offers as an important tool for characterizing the TTI.

## 2.1 Definition of the tundra taiga interface

The tundra taiga interface (TTI), as described by Callaghan *et al.* (2002), is one of Earth's greatest transition zones, stretching more than 13,400 km around the Northern Hemisphere. The TTI is regarded as the boundary between the dense boreal forest (taiga) composed of birch (*Betula spp.*), larch (*Larix spp.*) and evergreen conifers, and the Arctic tundra composed of permafrost regions containing low growing vascular plants as well as lichen and moss vegetation cover (Roberts *et al.*, 2006). The latitude at which the TTI occurs ranges between 70 and 55°N (Harsch *et al.*, 2009).

The study area for this project is situated within the High Subarctic Tundra eco-region of Labrador, Canada. The study area is representative of the most southerly region that is characteristic of this eco-region (Roberts *et al.*, 2006). Although the area is situated 3° latitude south of the optimal latitude for the boreal forest to Arctic tundra transition zone put forth by Callaghan *et al.* (2002), altitudinal conditions produce a transitional vegetation distribution example of the TTI eco-region.

Vegetation within the High Subarctic Tundra consists of three categories: forest, heath and barrens. Forest land cover occurs mostly in valleys and is composed of both deciduous and coniferous trees. In the valley the forest stands are in long axis dimensions ranging from 200 to about 1000 m. At higher altitudes, tree islands are present with a transect length of between 10 to 30 m (LHRG, 2008). A tree island is defined as an individual tree growing at the range edge for that species (Hermanutz, L., Professor, Memorial University, Personal communication, 2011). Tree islands exist in tree form or krumholtz form, the latter growing horizontally.

Heath is composed of low growth vegetation such as lichens, mosses, sedges and vascular plants. Barrens include rock-covered areas with little plant cover and high-altitude areas where conditions are too harsh for much vegetation to grow. Photographs taken at the study site show examples of forest and barrens (Figure 2.1) and heath (Figure 2.2) land cover categories. Note the change in land cover type as elevation increases.
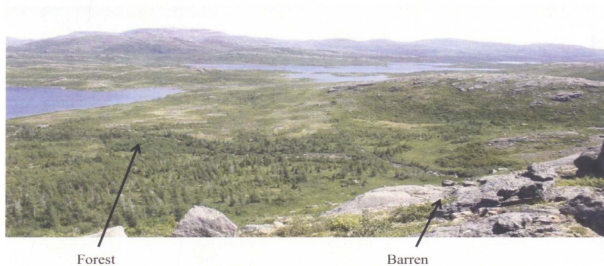


Forest                                        Barren

Figure 2.1: Photograph of study area representing Forest and Barren land cover. Photograph courtesy of Seth Loader, M.Sc. Memorial University, 2007.
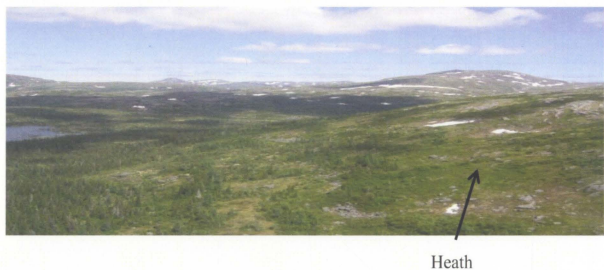


Heath

Figure 2.2: Photograph of study area representing Heath land cover. Photograph courtesy of Andrew Trant, M.Sc. Acadia University, 2009.

The TTI is a complex and dynamic ecostone that varies in both time and space (Grace *et al.*, 2002 and Skre *et al.*, 2002). Generally, the TTI is defined as the northern-most distributional limit of a group of species that have a common tree growth form (Payette *et al.*, 2001). However, there is some discrepancy in this definition at latitudinal and altitudinal limits of tree species distribution, because the form of the species is altered by environmental responses to changing climatic and topographic conditions, which cause species to grow as dwarfed shrubs, or horizontally (Payette *et al.*, 2001). In Labrador, this form of vegetation is more commonly referred to as krumholtz. The TTI being investigated for this project is a localized subarctic tree line, defined as the uppermost position of single-stemmed tree growth forms at least 2.5 m high (Lescop-Sinclair and Payette, 1995). This characteristic of trees in the transition zone is accounted for in the interpretation of the results obtained from the SAR images.

## 2.2 Remote sensing of the tundra taiga interface

Current remote sensing methods utilized to characterize land cover include multispectral vegetation indices, LiDAR and Radar. Each type of remote sensing system exploits a relationship between the at-sensor recorded EM energy and a particular characteristic of the land cover, such as height of vegetation, leaf chlorophyll content or dimensions of the vegetation components. The advantages and disadvantages of each of these methods are discussed in this section using examples from current literature.

## 2.2.1 Vegetation indices for characterization of the tundra taiga interface

Multispectral remote sensing methods for land cover characterization of a tree line environment utilize a vegetation index, the most standardized and widely accepted of which is the normalized difference vegetation index (NDVI). The NDVI most accurately represents vegetation when compared to six other indices (Lyon *et al.*, 1998). The NDVI equation uses the red and near-infrared bands of multispectral satellites to measure the leaf reflectance of green biomass in a landscape (Rouse *et al.*, 1973). The dominant factor controlling leaf reflectance is the concentration of pigments in the cells that make up the leaf structure, the most common of which are chlorophyll-a and chlorophyll-b (Gausman, 1974). The absorption spectrum of chlorophyll in healthy green vegetation is shown in Figure 2.3 and indicates that this pigment absorbs a high amount of red light, but reflects near infrared (NIR) light. When this observation is applied to multispectral satellite imagery in a normalized ratio equation, a NDVI image is produced (Equation 2.1).

$$NDVI = \frac{R_{NIR} - R_{red}}{R_{NIR} + R_{red}}$$

Equation 2.1

(Rouse *et al.*, 1973)

where the variable $R$ refers to the reflected EM energy of the respective wavelength of light as recorded by the satellite sensor.

The NDVI image ranges in values from negative to positive 1, where values from -1 to 0 represent non-vegetated land cover and values from 0 to 1 represent the amount of green biomass along an increasing scale.
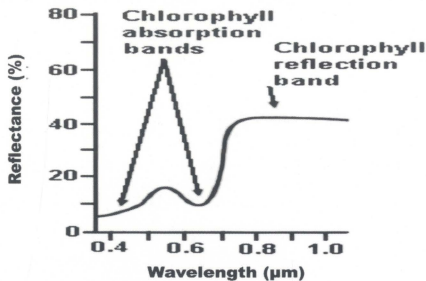
Figure 2.3: Typical spectral signature of healthy green vegetation.

Masek (2001) studied the expansion of forest land cover over time using co-located Landsat-1 (L-1) Multispectral Scanner (MSS) and L-7 Enhanced Thematic Mapper (ETM+) images. The analyzed images had a spatial resolution of 80 m. The study was conducted in two regions, near Richmond Gulf, Quebec, and Great Salt Lake, Northwest Territories. Images from 1974 and 1990 were acquired for the Richmond Gulf area, and for the Great Salt Lake area, images from 1972 and 2000 were acquired. The image pairs represented a 26 to 28 year time period over which forest changes could be investigated. NDVI images were created and the change in NDVI values over time were examined between the earlier and later date images. Results showed that the forest-tundra boundary could be accurately mapped using NDVI imagery. It was also found that there was no significant change in the distribution of forest, for either study area, over the specified time periods. One-pixel gaps in forest cover remained the same over time, which suggests

that if forest expansion occurred, that it could not be captured at an 80 m resolution. Masek (2001) recommended the use of more sensitive remote sensing approaches for the detection of forest expansion at a more detailed spatial scale, such as those with a higher spatial resolution.

In a similar study, Liu *et al.* (2005) investigated the use of Landsat images for their ability to detect tree line changes in the Changbai Mountains of China at a latitude of approximately 41° N. An L-1 MSS image from 1977 and an L-5 TM image from 1999 were acquired for this project. A NDVI image was created for each year and classified as forested or non-forested. The analysis was completed using 80 m and 30 m resolution. The results showed that there was no change in the tree line environment over the study period; however, there was an increase in the raw NDVI values between 1977 and 1999. This was attributed not to change in forest structure, but to anomalies caused by atmospheric interference, even after the necessary image corrections had been made. The atmospheric interference in the images was caused by the interaction of different wavelengths of light with particles in the atmosphere, such as dust, water vapour or clouds.

Through these studies, it has been demonstrated that the limited spatial resolution of Landsat multispectral imagery, combined with its sensitivity to cloud cover, cause difficulties in collecting data capable of producing a spatially continuous and temporally significant characterization of forest change over time. However, the data produced through these methods are proven to be useful when trying to characterize forested and non-forested land covers (as shown in Masek, 2001), because they are able to quantify the amount of green biomass. The information produced from the NDVI can be used as a

reference image, or a standard vegetation product, when investigating the use of other remote sensing data for forest characterization.

### 2.2.2 LiDAR remote sensing of the tundra taiga interface

Light Detection And Ranging (LiDAR) is an active airborne remote sensor that uses laser pulses (usually between 1 and 25 nm) to measure the elevation of objects on the Earth's surface (Shan and Toth, 2009). It is most often used to create digital elevation models, but can also be used to calculate the height of vegetation, allowing for description of particular land cover classes based on this characteristic. This section highlights studies that have been completed using LiDAR for forest classification.

Rees (2007) attempted to map a portion of the Arctic tree line in Finnmark, Norway using LiDAR data. The data were collected from the Optech ALTM3033 LiDAR sensor on board an aircraft and had a spatial resolution of 2 m. The LiDAR image covered an area of 126 km². Through this study, it was found that LiDAR data were appropriate for structural characterization of the forest edge if 'forest' was defined as "trees not more than 10 m from one another, with a tree being defined as at least 2 m tall." However, the author states that it would be impractical to use LiDAR data to characterize the entire circumpolar TTI due to the large amount of time and money required to collect and process it.

In a similar study, Korpela *et al.* (2010) investigated the ability of LiDAR intensity values to classify different tree species in a region of southern Finland. Images were acquired from two different airborne LiDAR sensors including the Optech ALTM3100 and the Leica ALS50-II with scanning footprints of 25 to 28 cm and 17 to 18

cm, respectively. Using these data, the authors obtained classification accuracies between 88 and 90% for both datasets. However, analysis of the potential fusion of both datasets revealed that intensity data for tree species classification varied between sensors for reasons that were unknown. This problem produces issues when trying to merge datasets and decreases the footprint area that can be covered by LiDAR data.

Due to its high spatial resolution and lack of atmospheric interference, LiDAR data show more promise than multispectral images when investigating tree line environments. There have, however, been concerns related to the feasibility of acquiring LiDAR data for the entire 13,400 km length of the TTI, as noted in the two studies presented above. As well, there are concerns related to the vertical accuracy of LiDAR data. Naesset (1997) found that the mean tree height calculated through LiDAR analysis underestimated the actual mean tree height recorded from ground truth data by 4.1 to 5.5 m with the standard deviation of this difference ranging from ±1.3 to ±1.6 m. The differences in mean tree height seen in LiDAR data can have a major impact if the objective is to characterize the spatial information about the canopy structure, as it may lead to misclassification of the TTI.

Recently, there have been significant advancements in LiDAR technology with the launch of ICESat's (Ice, Cloud, and land Elevation Satellite) LiDAR system: Geoscience Laser Altimeter System (GLAS). However, the data acquired from this satellite currently only provide sparse coverage of the Earth's surface (Van Leeuwen and Nieuwenhuis, 2010). With more research and development of this technology, perhaps it will be better suited in the future for the discrimination of land cover types on a larger, circumpolar scale.

## 2.2.3 Radar remote sensing

Radar is an active remote sensing system that emits millimetre- to metre- length waves and records the intensity of backscatter that is returned to the sensor. The amount of EM energy that is recorded at the sensor is related to the shape and structure of the phenomena being imaged (Herold *et al.*, 2004), and varies for different land cover types based on these characteristics. Variation in tone across a radar image may also be due to differing dielectric properties, often dependant on the water content of the materials being investigated (Freeman, 1998). Radar images can provide information that may help better characterize the tundra taiga interface when compared to multispectral and LiDAR data.

Ranson *et al.* (2004) tested the ability of five datasets from different sensors to characterize the surface and vegetation structure changes aross the tundra taiga interface in a region of Siberia, Russia. The datasets included four multispectral image sets (L-7 ETM+, IKONOS, MISR, and MODIS) and one R-1 image set consisting of five standard mode images with varying incidence angles. L-7 ETM+, MISR red band multi-angle data, MODIS time series data, and R-1 large-incidence angle images all showed significant differences between the spectral signatures or backscattering seen in tundra and taiga environments. The implication of this research, as stated by the authors, is that "global coverage available from RADARSAT may be used for analysis where high resolution is required and cloud cover or low illumination precludes the use of Landsat-like data" (Ranson *et al.*, 2004 from p. 294).

R-2 data, available since 2007, are the successor to R-1, and while they still offer data that are analogous to R-1 products, they also offer higher-resolution, multi-polarized data. The ability of these data to characterize the TTI has not so far been investigated, yet

provides a means to supersede or complement existing remote sensing products for characterizing forest-tundra environments, such as multispectral and LiDAR products, as discussed above.

*2.2.3.1 Study area vegetation composition and radar backscatter*

This research focuses on the Mealy Mountains study area. Within the study area, three types of land cover are of interest: boreal forest, Arctic tundra, and water. The boreal forest region, or taiga, is composed of larger deciduous (birch, willow and larch) and coniferous (larch, black spruce, white spruce and balsam fir) trees and shrubs whose branches and leaves produce a thick canopy cover. In general, there is variation of tree heights in taiga land cover due to availability of nutrients, soil composition, drainage patterns as well as inter- and intra-species competition (Loehle and LeBlanc, 1996).

Arctic tundra land cover comprises vascular plant species that lightly blanket the ground and do not vary considerably in height, as well as exposed bedrock, which may vary in surface height due to fractures and glacial scarring (Clarke *et al.*, 2000).

Water bodies are otherwise planar surfaces that only have slight changes in roughness when affected by wind. Water will not be considered when defining the TTI, but is taken into account as a means of delineating water from land.

Sieber (1985) and Richards (1985) have shown that the backscatter intensity of different land cover types is fundamentally related to vegetation characteristics such as surface roughness, canopy cover, tree density and height. Thus, the differences in these characteristics as noted above should allow for delineation between the land cover types within the study area. These are the characteristics that will be exploited during analysis

of R-2 radar imagery in order to delineate Arctic tundra (non-forest) from forested land cover.

Strong differences in backscatter values of land cover features are also dependant on specifications of the radar sensor, including incidence angle, polarization, wavelength and spatial resolution. Ranson *et al*. (2004) found that horizontal like-polarized (HH), C-band radar with high incidence angles are suitable for exploiting differences in the size and structure of tundra vs. taiga land cover. These results are also emphasized in Verbyla (2001), in which the potential of European Remote Sensing (ERS-2) and R-1 radar imagery to detect spring leaf flush in the Alaskan boreal forest region was examined. The images were taken before and after the spring flush during the 1997-1998 and 1998-1999 spring seasons, respectively and re-sampled to a spatial resolution of 25 m. The vertical like-polarized (VV) ERS-2 images, with incidence angles between 20 and 26 degrees, showed no consistent difference between before- and after-spring flush images. However, the R-1 images with HH polarization and incidence angles between 24 and 31 degrees, demonstrated an increase in the mean backscattering value of the before- and after-spring flush images. The effect of incidence angle is seen only in the HH images. The outcomes of this study are attributed to horizontally polarized energy interacting with tree branches and leaves rather than with tree trunks.

The studies noted above are useful to establish guidelines of specifications within which to conduct the development of a R-2 -derived vegetation product, so that the best possible results can be produced. The four radar system specifications of most concern are wavelength, incidence angle, spatial resolution and polarization. C-band radar will be

used, as this is the only wavelength available from R-2 and has been proven effective in forest density mapping.

Where possible, image modes with an incidence angle of at least 25° are used because they have been shown to represent the best separation between forested and non-forested areas. The combination of the RADARSAT C-band wavelength (5.56 cm) into equations 2.2 and 2.3 suggests that surface roughness on the order of 0 to 0.24 cm and 1.39 cm and greater can be discriminated from each other with an incidence angle of 25°. However, the smooth and rough criteria with an incidence angle of 45° (R-1's S7 mode) are 0 to 0.34 and 1.93 cm and greater, respectively. In the context of the TTI, barren tundra components are expected to be identified with the smooth surface ($h_{smooth}$) causing specular backscattering, while the taiga land cover is characterized as having a rough ($h_{rough}$) surface texture which would cause diffuse backscattering.

$$h_{smooth} < \lambda/25 \cos \theta \qquad\qquad \text{Equation 2.2}$$
$$h_{rough} > \lambda/4.4 \cos \theta \qquad\qquad \text{Equation 2.3}$$

(Jensen, 2007)

where $\lambda$ and $\theta$ represent the wavelength and incidence angle, respectively. The heights of a surface roughness that will tend to produce a specular backscattering (low brightness values) are represented by $h_s$, while surface roughness values that result in a diffuse backscattering (high brightness values) are represented by $h_r$. The taiga (forest) landscapes found in the study area all have a ground relief that is greater than 1.39 cm, so it is expected that these features will cause high returns relative to landscape surfaces that

have a lower relief, such as lichens, mosses and shrub leaves found in tundra (non-forest) landscapes. The surface roughness-related variations form the basis to investigate radar image brightness as a means to discriminate between forested, at least 2.5 m high (Lescop-Sinclair and Payette, 1995), and non-forested land cover at the TTI.

The two remaining specifications, spatial resolution and polarization, are not as easily conceptualized due to lack of literature in these areas, however, both polarization and spatial resolution have been identified as parameters that can enhance detection of forest and non-forest areas for other radar wavelengths and are worth investigating in relation to C-band R-2 products.

A higher spatial resolution generally leads to a better differentiation of forest canopy characteristics. For example, Santoro *et al.* (2009) analyzed the backscatter characteristics of a series of images captured by the Phased Array type L-band Synthetic Aperture (PALSAR) Radar sensor aboard the Advanced Land Observing Satellite (ALOS) for their ability to delineate forest growth stages in a boreal forest region of southern Sweden. The authors investigated the backscatter associated with forest growth stages for a series of images with spatial resolutions that ranged between 20 and 50 m. The study indicated that higher spatial resolution images produced better class separation results between forest growth stages. Polarization was also investigated in this study, concluding that cross-polarized backscatter is more sensitive than like-polarized backscatter to different forest growth stages. Furthermore, Rees (2007) found that tree line classification results were highly dependent on the spatial resolution and the canopy density of the forest landscape. Fine resolutions (about 10 m) captured forest and non-

forest areas as heterogeneous features while at coarse resolutions (about 30 m) the two classes were represented as homogenous features.

For the purposes of this thesis, all spatial resolution and polarization modes available through R-2 have been investigated in order to establish the most useful R-2 image mode for characterizing tree line information. In terms of spatial resolution, the available modes are ultra fine, fine and standard, which represent nominal spatial resolutions of 3, 9 and 30 m, respectively. For polarization options, R-2 images are available in both single like-(HH or VV) and cross-polarization (HV or VH) as well as dual and quad polarization, in which a combination of two or more like- and cross-polarizations are imaged at the same time.

## 2.3 Extracting land cover information

Raw backscatter intensity values and texture transforms are two methods commonly used to extract numerical information that is characteristic of a particular land cover. The first of these tasks is utilized for radiometric calibration, while the second requires an in-depth investigation of analyses parameters such as filter types and sizes.

### 2.3.1 Backscatter analysis

Backscatter refers to the interaction of the radar signal with phenomena on the Earth's surface. Different types of backscatter interaction affect the intensity of radar energy that is returned to the sensor, thus influencing the representation of a particular phenomenon on the resulting radar image. There are three main types of backscattering mechanisms that are known to occur: specular, corner and volume backscatter. Specular

backscatter occurs when the emitted electromagnetic energy interacts with a smooth surface (i.e. asphalted road and calm water surfaces) and is reflected away from the sensor. Very little to no energy is received at the sensor, thus producing a dark image backscatter value. Corner backscattering happens when the energy bounces off the Earth's surface where, after it has encountered a vertical structure (i.e. urban building or tree trunk), it is redirected towards the sensor (this phenomena is also referred to as double bounce). The image backscatter values are high for regions where corner backscattering occurs. Finally, volume backscatter refers to the interaction of the emitted energy with a rough surface (i.e. vegetation canopies that have varying density, height, tree and branch spacing, etc.). In this case, the energy is scattered in multiple directions, away and towards the sensor, resulting in varying backscatter values in the medium greyscale range.

Backscatter analysis is an investigation of the statistical differences between backscatter (i.e. intensity) values of two or more different land cover types. Backscatter differences are most often expressed as a backscatter signature, whereby the mean and standard deviation of the backscatter response for differing land cover classes are expressed on a plot (as in Ranson *et al.*, 2004). Analysis such as this can also provide information on optimal radar specifications when an image set is available that has variations of a particular specification, such as polarization, incidence angle and spatial resolution, as seen in Santoro *et al.* (2009)

### 2.3.2 Texture analysis

Radar images are normally wrought with high frequency speckle noise that may interfere with backscatter-based class differentiation. Typically, texture images are created from the SAR backscatter image to minimize such interferences. Texture images take into account the spatial variability of brightness values across the images, thus decreasing noise and increasing the amount of useful information that can be extracted from the image (Tsymbal *et al.*, 2005). Two categories of texture filters can be effective. First order texture is calculated directly from the backscatter intensity image using a filter of size n x n that moves in a box-car like manner throughout the image, where 'n' is the number of filter elements matching the image pixels. First order texture variables include statistics such as coefficient of variation, energy, entropy, kurtosis, mean, skewness and variance (Dekker, 2003; Haack, 2007; Luckman *et al.*, 1997). Second order texture images are calculated based on a grey-level co-occurrence matrix (GLCM), which is a derivative of the backscatter intensity image. The GLCM represents the relationship of a reference pixel to its 'n[th]' neighbouring pixel. GLCM-derived textures may include contrast, correlation, dissimilarity, entropy, homogeneity, inverse difference and GLCM mean (Kurvonen and Halikainen, 1999; Luckman *et al.*, 1997; Ulaby *et al.*, 1986). First and second order texture filters can be directional or isotropic, in order to enhance some or all landscape feature orientations, respectively.

Ulaby *et al.* (1986) classified land cover and forest type using images from the Seasat-SAR and shuttle image radar-A (SIR-A) for parts of the northern United States, Mexico and South America. The land-use categories included in this study were water, forest, pasture, urban, and cultivated, SIR-A data were recorded in L-band (23.5 cm

wavelength), HH polarization, and the image analysis was based on a 40 m spatial resolution image. A maximum likelihood classification algorithm was applied to the backscatter intensity image as well as first and second order texture images. The raw backscatter image yielded an accuracy of about 58% for forest, while the contrast and inverse moment texture images provided an accuracy of 88%. An accuracy of 93% for the forest class was obtained when the backscatter intensity and contrast image were combined. Furthermore, Haack (2007), found that texture calculated using a first order variance texture improved the classification accuracy of land cover for R-1 images of Katmandu, Nepal by about 20% compared to the original radar backscatter image.

Luckman *et al.* (1997) classified forest growth stages using C-band SAR images acquired from the Convair 580 airborne system for the Tapojos region of the central Amazon forest in Brazil. The spatial resolution of the images was 6 m and the dataset contained two images, one with HH and one with VV polarization. Each image was classified into one of five categories ranging from clear-cut to virgin forest. The raw backscattering values for each image were investigated as well as two texture measures, a first order coefficient of variation (CV) and a second order GLCM-derived contrast. The analysis showed that there was no significant difference between the mean backscatter amplitude of the growth classes. Although it was hypothesized, based on another study of the same region (Grover and Quegan, 1995), that the C-band radar signal does not penetrate far into a vegetation canopy and as a result, the backscattering for mature forest is similar to that of regenerating forest, agricultural crops, or even moist bare soil. The CV texture measure performed the best for both polarization images compared to the raw backscattering and the contrast texture measure. The two texture measures were better at

distinguishing between regeneration classes than backscattering alone, but the only statistically separable classes were virgin forest classes and all other regeneration classes combined.

Dekker (2003) applied multiple texture measures to ERS-1 SAR images for the mapping purpose of updating an urban area in the Netherlands. The results found that the classification of land cover clusters (which included forest) could be improved using texture measures. Twenty-six texture measures were tested for this purpose. Of those twenty six texture measures, first order mean and variance performed the best.

Kurvonen and Hallikanen (1999) also explored the use of the European Remote sensing satellite (ERS-1) and the Japanese Earth Resource satellite (JERS-1) SAR data to classify land cover and forest types in a boreal forest region of Finland. Using the backscattering image and second order texture images, five land cover types were classified, including water, gravel, forest, mire and open bog. The highest overall classification accuracy (65%) was obtained using the inverse moment second order texture image. The highest class accuracy was 70% for water and the lowest was 62% for mire. An anomaly noted by the authors during classification was that young new growth forest and shrubs within agricultural land were often misclassified as forest.

These studies demonstrate that texture variables applied to radar images produce superior results for land cover delineation compared to those that investigate raw backscatter values only. The studies also highlight the texture measures that may be appropriate for enhancing statistical differences between forest and non-forest land cover, which are of interest in this project.

## 2.4 Geostatistical methods in remote sensing

When backscatter and texture information are considered, it is also important to understand the spatial relationships that are taking place between data points both on the ground, and in the imagery being analyzed. For example, Haack (2007) stated that the effectiveness of a window size was most likely related to the variability and spacing of ground features, including field size and building density. Furthermore, Wu and North (2001) state that the half width of a texture filter is related to the minimal visible feature size at the corresponding scale. Given a 7x7 cell filter on an image with an image spatial resolution of 30 m, a minimum feature size of 105x105 m (i.e. 7/2*30=105) would be detectable.

A practical method to investigate the spatial relationships within a dataset is through geostatistics. Geostatistics applies theories of random processes and statistical inference to geographical phenomena. One of the main theories of this particular school of thought is that there are different scales of spatial variation within a dataset and that all data are spatially dependant (i.e. data values that are closer together are less variable than those which are further apart). Most geostatistical approaches interpolate areas of datasets that cannot be sampled using statistical inferences related to how data values are spatially correlated with neighbouring data values (Babish, 2006). Remote sensing datasets already contain a large amount of closely spaced and regularly gridded information. Therefore, geostatistical methods offer an ideal format for assessing the spatial variability of the grey level values found within an image (Assia and Aichouche, 2004).

A remotely-sensed image is considered a spatial dataset, and as such, the spatial characteristics associated with these types of datasets should be considered. The two most

common spatial characteristics are spatial heterogeneity and spatial dependence. Spatial heterogeneity, also referred to as spatial non-stationarity, occurs when the parameters describing the data vary from place to place. Spatial dependence means that data values which are spatially closer together are less variable than those which are further apart. A description of these characteristics provides important information about which texture measures and windows sizes may be appropriate for a given remotely sensed image and is most often described using variogram parameters (Getis and Ord, 1992). Examples of the use of each of these parameters with respect to remote sensing data are given below.

Variogram analysis involves the construction of a semi-variogram, which is a plot that expresses the empirical data's semivariance along the y-axis and the distance between data values along the x-axis. Semivariance is expressed as a measure of the average squared dissimilarity between data pairs in a defined region. A theoretical variogram model is then fit to the empirical semi-variogram in order to represent its structure and characteristics. The point at which the variogram model reaches a maximum semivariance, also known as the sill, is indicative of the distance at which there is minimal spatial autocorrelation between the image pixels (Smith *et al.*, 2007). When considering the characteristics of a particular land class, the sill can inform a decision on the maximum filter size that should be used during texture analysis (Franklin *et al.* 1996; Hyyppä and Hyyppä, 2001; Karl and Maurer, 2010*)*.

## 2.5 Conclusion

Radar images show great promise to be used as a consistent and reliable data type in order to characterize the nature and dynamics of the TTI. Through the investigation of the ecological and spatial aspects of the land cover classes that are found within the study area, it is hypothesized that forest, non-forest and water will possess different radar backscattering properties, which will allow for the delineation and analysis of the TTI using R-2 products. A major component that will be considered in order to create the best possible separation between land cover classes is texture information. The main focus of this research is to find an appropriate texture measure and window size that most accurately represents the TTI for the particular dataset at hand. The underlying spatial relationships and characteristics that exist between pixel values that represent different land cover types can be understood using geostatistical approaches adapted to the radar dataset. Building on the successes of R-1 in forestry applications (Ranson *et al.,* 2004), this research is intended to create the means to move to R-2 as a main source of data for monitoring of the tree line in northern regions.

# Chapter 3: Data

## 3.0 Introduction

The success of this study in part depends on the availability of near anniversary date (i.e. recorded on the same date but not necessarily on the same year) NDVI and radar images. In order to meet these requirements, an acquisition plan for R-1 and R-2 data was compiled, and the imagery subsequently acquired. Ancillary data for this project include *in situ* field data, short-term weather data and a digital elevation model (DEM).

## 3.1 Multispectral images

The NDVI is calculated using the red (0.6-0.7 µm) and near infrared (NIR) (0.7-0.8 µm) bands from multiple spectral images. Three NDVI images, from September 2008, August 2005 and July 2001 are used for this project. Prior to the NDVI equation being applied, the red and NIR band image is atmospherically corrected. The images that are utilized to create the NDVIs all come from different sensors, which may have different radiometric properties, rendering them unreliable for multi-date analysis. In order to correct for this, a multi-date image calibration was applied using the pseudo invariant feature (PIF) method (Schott *et al.*, 1988). PIF's are features that are assumed to have a constant spectral reflectance over time, which in the NDVI images include glaciers, deep water bodies and bare rock land cover. The 2001 NDVI was used as the baseline to calibrate the 2005 and 2008 NDVI images. Forty-six PIF's were selected, from which a linear regression function, and corresponding offset and gain values were

derived between the baseline and each of the other images. These calibration equations were subsequently applied to the 2005 and 2008 NDVI.

A georectification is also applied to the images using the North American datum 1983 for UTM zone 22 row U. The Landsat 7 products from September 20, 2001 are georeferenced and thus used as the reference for georectification of the remaining multispectral images. The NDVI product was resampled to 30 m to match the spatial resolution of standard mode R-1 and R-2 products. The images also exist in their original spatial resolution and will be useful for comparison to R-1 and R-2 fine mode images as well as R-2 ultra-fine mode images. Notable specifications of NDVI images are presented in Table 3.1.

Table 3.1: Specifications of NDVI images.

| Date | Platform and sensor | RMS (pixel) | Initial spatial resolution (m) | Resampled spatial resolution (m) |
|------|------|------|------|------|
| Sept. 20, 2001 | Landsat-7 ETM+ | N/A | 30 | N/A |
| Sept. 06, 2005 | QuickBird multispectral | 0.761 | 2.4 | 30 |
| Aug. 30, 2008 | SPOT HRVIR | 0.647 | 10 | 30 |

### 3.1.1 Water mask development

The near infrared band from each multispectral image is used to create a water mask. Shallow water absorbs near infrared light and thus, when imaged, lakes and rivers appear as the darkest pixel values. This characteristic is contrasted on land, from which near-infrared light is strongly reflected. Land and water can be distinguished numerically

by examining the near infrared image's histogram. The water-land threshold value is determined where, on the histogram, the brightness values of lowest occurrence between water and land distribution functions are present (Mather, 2004). It is then used to reclassify the image into a binary product in which water and land are represented as 0 and 1 respectively. The 2005 Quickbird water mask image is presented in Figure 3.1. The water mask will be applied to any output radar product that is created through this project in order to focus the analysis on land features.
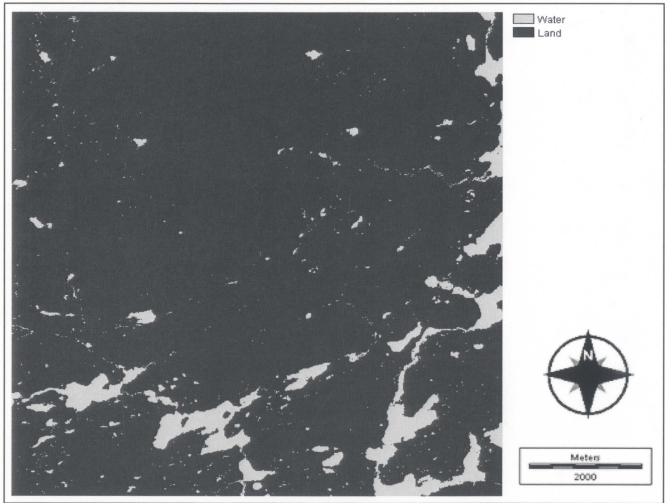


Figure 3.1: Water land mask calculated from the SPOT 2008 image of the study area. Note that the mapped area is 8 x 8 km.

## 3.2 SAR Imagery

Fourteen R-2 SAR images were acquired between August 21 and September 24, 2009. The image set consists of five 'fine' mode images, five 'standard' mode images and four 'ultrafine' mode images, which differ in their spatial resolution (Table 2). Concurrently, the dataset includes like-, cross- and quad-polarized images, and a range of incidence angles.

A set of six RADARSAT-1 (R-1) images was also acquired. The main R-1 image acquisition criteria were that they match the NDVI image dates. Table 3.3 shows the R-1 and NDVI image dates, as well as the R-1 image specifications.

All multispectral and radar images were recorded within a two month time period (August 3 to September 26). A time line is presented in Figure 3.2 to illustrate data continuity between the NDVI and radar imagery. The acquisition of all data within this time frame minimizes the effects of seasonal variations on the vegetation cover, which could potentially affect the analysis results. Same year NDVI and R-1 images, as well as R-1 and R-2 images have comparable spatial resolutions.

Table 3.2: Specifications of the R-2 SAR images.

| Mode | Spatial resolution (m) | | Polarization | Incidence angle (degree) | Date (2009) |
| | Range | Azimuth | | | |
|------|-------|---------|--------------|--------------------------|-------------|
| F2   |       |         | VV           | 39.55                    | Sept. 27    |
| F4   | 10    | 9       | HH           | 43.61                    | Sept. 13    |
| F21F |       |         | HV           | 35.71                    | Sept. 3     |
| F5   |       |         | VH           | 45.44                    | Sept. 7     |
| FQ19 | 10    | 6       | HH/HV/VH/VV  | 38.51                    | Sept. 17    |
| S3   |       |         | VV           | 30.96                    | Sept. 10    |
| S6   | 25    | 28      | HH           | 41.7                     | Sept. 24    |
| S7   |       |         | HV           | 44.86                    | Sept. 6     |
| S4   |       |         | VH           | 34                       | Sept. 10    |
| SQ21 | 25    | 28      | HH/HV/VH/VV  | 40.34                    | Sept. 20    |
| U2   |       |         | VV           | 30.8                     | Sept. 23    |
| U27  | 3     | 3       | HH           | 48.71                    | Sept. 14    |
| U17  |       |         | HV           | 42.4                     | Aug. 27     |
| U27  |       |         | VH           | 48.71                    | Aug. 21     |

Abbreviations: Mode- F=fine, FxxF= fine far, S=standard, U=ultrafine, SQ=standard quad-polarized, FQ= fine quad-polarized; Polarization- HH= like horizontal polarized, VV= like vertical polarized, HV= cross horizontal vertical polarized, VH= cross vertical horizontal polarized.


Table 3.3: Specifications of the R-1 SAR images.

| Mode | SR (m) | IA (degrees) | Date           | Matching image and date     |
|------|--------|--------------|----------------|-----------------------------|
| F1   | 8      | 38.4         | Sept. 26, 2005 | NDVI on Sept. 06, 2005      |
| F3N  | 8      | 41.52        | Sept. 12, 2009 | R-2 on Sept. 13, 2009       |
| S1   | 30     | 30.93        | Aug. 08, 2001  | NDVI on Sept. 20, 2001      |
| S4   | 30     | 34.26        | Sept. 15, 2009 | R-2 on Sept. 10, 2009       |
| S5   | 30     | 39.24        | Aug. 03, 2008  | NDVI on Aug. 30, 2008       |
| S7   | 30     | 46.96        | Sept. 07, 2008 | NDVI on Aug. 30, 2008       |

Abbreviations: mode- FxN=fine near, S= standard, F= fine; specifications- SR= spatial resolution, IA= incidence angle.
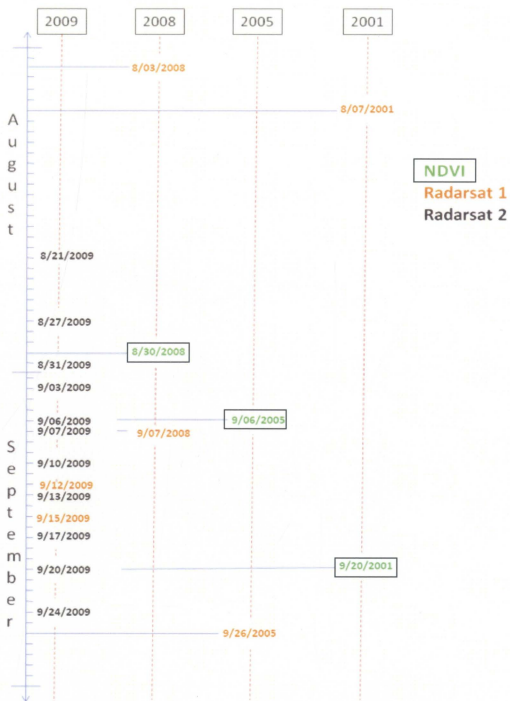
Figure 3.2: Timeline of image acquisition dates.

**3.3 Field data**

The field data for this study were collected by members of the Labrador Highlands Research Group (LHRG), in conjunction with the PPSA IPY project number 2006-SR-1-CC-027 from 2006 to 2011. Field data were collected in July 2007 and August 2008 (LHRG, 2010). The records consist of GPS coordinate-tied information for land cover types including forest, heath and barren, as well as land cover for 500 and 1000 m transect lengths distributed throughout the study area. The field data also contain measurements on estimated tree height in metres, patch size and location of tree islands, and canopy density in percent cover.

The two sets of field data are used to create two distinct point data sets. Each data set contains at least 30 non-forest and 30 forest samples. The data set was split into two groups at random, one to guide the analysis and the other to validate the results. The geographical location of all field points and the corresponding land cover classes are displayed below in Figure 3.3, with the 2008 NDVI as the background image.
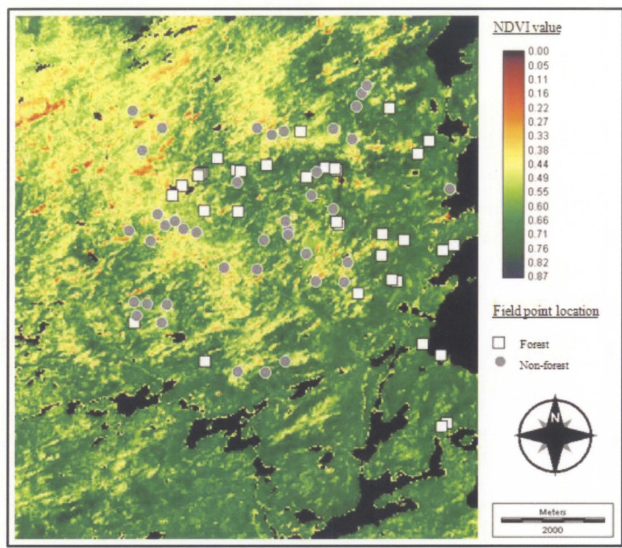
Figure 3.3: Location of field points and 2008 NDVI image.

## 3.4 Short-term weather data

Short-term precipitation information was collected for a ten day period prior to

the date of image acquisition of each SAR image from the National Climate Data and

Information Archive (Table 3.4). The archival precipitation data were compiled for the

Happy Valley-Goose Bay (Environment Canada, 2010a) and Cartwright (Environment

Canada, 2010b) weather station. The precipitation data are used in order to complete a

qualitative assessment of the effects of surface moisture on the analysis results. Past

studies have suggested that the backscatter signature of land cover is affected by moisture

content (Monsivais-Huertero *et al.*, 2010). The moisture of a radar target increases its dielectric constant, which causes the backscattering to increase. The study area is situated about 120 km north east of the Happy Valley-Goose Bay weather station and about 120 km west of the Cartwright weather station.

Table 3.4: Cumulative and average precipitations recorded 10 days prior to each image.

| Image number | Satellite | Date | $CP_{HVGB}$ | $CP_{CWT}$ | Average (mm) |
|---|---|---|---|---|---|
| 1 | R-2 | 8/21/2009 | 20.8 | 19.9 | 20.4 |
| 2 | R-2 | 8/27/2009 | 83.2 | 49.6 | 66.4 |
| 3 | R-2 | 8/31/2009 | 73.0 | 58.4 | 65.7 |
| 4 | R-2 | 9/3/2009 | 79.8 | 63.8 | 71.8 |
| 5 | R-2 | 9/3/2009 | 79.8 | 63.8 | 71.8 |
| 6 | R-2 | 9/6/2009 | 37.6 | 40.1 | 38.9 |
| 7 | R-2 | 9/7/2009 | 21.0 | 32.6 | 26.8 |
| 8 | R-2 | 9/10/2009 | 15.8 | 22.9 | 19.4 |
| 9 | R-2 | 9/10/2009 | 15.8 | 22.9 | 19.4 |
| 10 | R-1 | 9/12/2009 | 16.4 | 20.5 | 18.5 |
| 11 | R-2 | 9/13/2009 | 24.2 | 28.5 | 26.4 |
| 12 | R-2 | 9/14/2009 | 81.8 | 83.6 | 82.7 |
| 13 | R-1 | 9/15/2009 | 82.2 | 106.4 | 94.3 |
| 14 | R-2 | 9/17/2009 | 82.2 | 105.4 | 93.8 |
| 15 | R-2 | 9/20/2009 | 88.6 | 101.8 | 95.2 |
| 16 | R-2 | 9/24/2009 | 84.2 | 105.9 | 95.1 |
| 17 | R-1 | 9/7/2008 | 15.4 | 21.0 | 18.2 |
| 18 | R-1 | 8/3/2008 | 21.8 | 19.2 | 20.5 |
| 19 | R-1 | 9/26/2005 | 45.2 | 47.3 | 46.3 |
| 20 | R-1 | 8/2/2001 | 29.2 | 27.1 | 28.2 |

Abbreviations: CP=cumulative precipitation, HVGB= Happy Valley - Goose Bay, CWT= Cartwright.

## 3.5 Digital Elevation Model

The digital elevation model (DEM) available for the study area is a *Canada digital elevation data* level 1 product from the Centre for Topographic Information

(Natural Resources Canada). The product has a spatial resolution of 18 m and a vertical accuracy of 10 m. The DEM is used during orthorectification of the SAR data and for validation of the final product. The DEM is also used in the creation of radar layover and shadow masks, and to extract landscape parameters. These are used to assess the effects of topographical variables on the radar-derived product.

### 3.5.1 Layover and shadow mask development

A layover mask and a shadow mask are created for each radar image using the digital elevation model along with the image range and azimuth information contained within the metadata. The layover and shadow masks are used when assessing the accuracy of the final radar-derived vegetation product because the areas that produce radar backscatter anomalies are isolated. The only area of concern where these anomalies may occur for this study area are in the top northwest corner where there are abrupt slopes and changing terrain elevations. Areas such as this, which are known to be susceptible to layover and shadow during image acquisition, may lead to inaccurate backscatter values that do not represent the true land cover type (Small *et al.*, 1997). The application of a layover and shadow mask will reduce these effects.

### 3.5.2 Landscape parameters

The DEM is also used to derive landscape parameters and assess sources of error in the final product. A separate raster image for slope and aspect is developed. Terrain slope is calculated from the DEM using an average maximum technique (Burrough and McDonnell, 1998), whereby the maximum terrain elevation change from one cell to its

neighbouring cells is calculated using Equation 3.1 and a 3 x 3 cell neighbourhood. Slope is calculated in degrees and classified into three classes of low (0 to 15º) medium (15 to 30º) and high (≥30º). The final slope product is shown in Figure 3.4.

$$slope = \arctan \sqrt{[\Delta z/\Delta x]^2 + [\Delta z/\Delta x]^2} \times 180/\pi$$  Equation 3.1

where $z$ = rise in height $x$ = run.
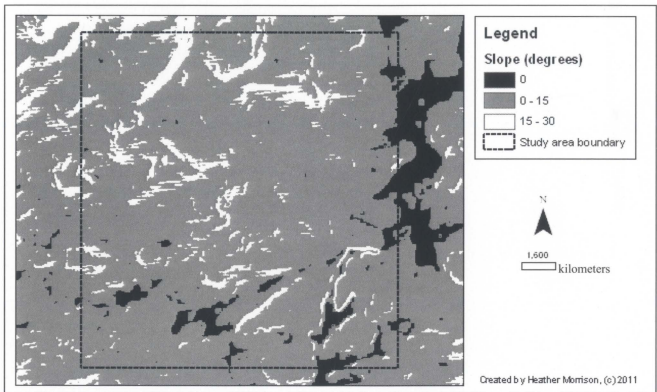


Figure 3.4: Classified slope product derived from digital elevation model.

The aspect denotes the downslope direction of the maximum terrain elevation change of each cell to its neighbours. Aspect was first calculated using cardinal directions and then reclassified as per the incidence angle of the radar image used to create the final vegetation product. The aspect is classified as foreslope, eastward, backslope and westward in relation to the incident radar beam. For an image acquired with a descending orbit and an incidence angle of 45º the aspect would be classified according to Figure 3.5.
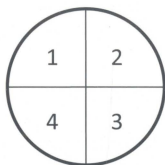
Figure 3.5: Aspect classification for image with descending orbit and incidence angle of 45°. 1: foreslope, 2: eastward, 3: backslope, 4: westward.

# Chapter 4: Methodology

## 4.0 Methods

The objective of the remote sensing analyses is to convert data to information. Some processing, such as geometric, atmospheric and radiometric correction are tailored for the given satellite sensor. The information extraction phase must consider the data-type and the desired project outcome. The methods outlined in this section will be utilized to answer three main research questions:

- Which texture measures, when applied to radar imagery, provide the best delineation between Arctic tundra and taiga environments?

- Which R-2 mode provides the most enhanced characterization of the tundra taiga interface (TTI)?

- Can radar remote sensing be utilized as an appropriate measure to delineate the TTI in a manner that can supersede or match current multispectral-based methods using the normalized difference vegetation index?

The analysis process, as illustrated in Figure 4.1, consists of three major sections, including image processing and radar vegetation product development. The first part of the methods, image processing, was focused on preparing the radar data. Processing was applied to R-1 and R-2 imagery, as the NDVI images were already corrected. The second part of the methods, the R-2 product development stage, was more focused on producing information from the data. This includes two phases: the R-1 and R-2 image investigation phases. The methods carried out within each stage are explained in the following section.

```
┌─────────────────────┐      ┌─────────────────────┐      ┌─────────────────────┐
│   Data processing   │ ──→  │    Data analysis    │ ──→  │  Results evaluation  │
└─────────────────────┘      └─────────────────────┘      └─────────────────────┘
```

**Image processing**
• Radiometric calibration
• Geometric rectification
• Rescaling
• Sub-setting
**Image investigation**
• Accuracy of NDVI
• Backscatter analysis
• Variogram analysis

**Texture analysis**
**Product development:**
**Selection phase (R-1)**
• Descriptive statistics
• K-S test
• Linear regression and correlation
• Selection of optimal texture measure
**Application phase (R-2)**
• K-S test
• Linear regression and correlation
**Radar derived vegetation variable**

**Evaluation of derived vegetation product**
- Independent evaluation set

Figure 4.1: Analysis process and corresponding methods.

## 4.1 Data processing

The R-1 and R-2 satellite data were processed to eliminate effects imposed on the product from satellite scaling values as well as radiometric noise and geometric distortions. Four tasks were performed during pre-processing, included radiometric calibration, orthorectification, image rescaling and image sub-setting (Refer to Figure 4.1). These corrections were necessary to R-1 and R-2 image data analysis for the pixel values to be compared across multiple dates and image modes. In addition, geographical coverage of the R-1 and R-2 products had to match NDVI images

### 4.1.1 Radiometric calibration

A scaling offset and gain was applied to radar images in order to enhance their dynamic range. However, the scaling offset and gain differs for each image, or scene, that is acquired. In order to compare brightness values across datasets, the brightness values

had to be calibrated such that each image displayed with the same dynamic range. The images acquired for this project were 'single look complex' product type, which contained both real (I) and imaginary (Q) parts that must be combined in order to create a calibrated backscatter image. Three types of information were required to complete a radiometric calibration: an array layer of local incidence angles, a sigma backscatter look-up table (LUT), and the I and Q values. The array layer of incidence angles was created using the satellite orbital and offset information contained in the metadata of each radar image. The LUT was available in an ancillary file within the product file. When the above variables were combined using Equation 4.1, a calibrated backscatter image was produced.

$$\sigma_{ij} = 10 \times log10\left(\frac{DN_I \times DN_I + DN_Q \times DN_Q}{A_j \times A_j}\right) + 10 \times log10(\sin(\theta_j))$$

Equation 4.1

(PCI Geomatics, 2011)

where $\sigma_{ij}$ is the output backscatter coefficient for scan line $i$ and column $j$, DN represent digital number, such that $DN_I$ is the input image $I$ value at $(i, j)$ and $DN_Q$ is the input image $Q$ value at $(i, j)$, $A_j$ is the LUT value for pixel $j$, and $\theta_j$ is the incidence angle table value for column $j$.

### 4.1.2 Georectification

Georectification applies spatial references to a dataset, relating it to a particular location on the Earth's surface. This process rectifies the data in the x and y planes. An

orthorectification incorporates topographical information from a digital elevation model to rectify the data in the $z$ plane. Each image was georectified and orthorectified using the radar specific mathematical model included in each image's metadata. All images were referenced to the Earth's surface using the North American Datum 1983 (NAD 83) and the Universal Transverse Mercator (UTM) coordinate system for zone 22, row U, so as to correspond with the reference system of the NDVI images. Also during rectification, radar images were transformed from slant range to ground range and radiometric terrain corrections were applied in order to locate the areas affected by radar shadow, layover and foreshortening.

The effectiveness of orthorectification is evaluated by the average root mean square (RMS) error. This parameter indicates how much the corrected image deviates from selected ground control points. For example, an RMS of 0.3 pixels for an image with a spatial resolution of 30 m indicates that the image, on average, deviates by 9 m from the reference system. As a guideline, the RMS value should not exceed half the length of a pixel. The radar specific math model incorporates tie points contained in an image's metadata in order to rectify the imagery, however, where necessary, ground control points (GCPs) are added manually in order to enhance the accuracy of the rectified product. GCPs are points for which the geographic coordinate is known from reference maps or field data.

### 4.1.3 Image rescaling

Pixels on the radar images are represented in units of amplitude for the intensity of backscatter recorded at the sensor. In order to apply the image processing with 8-bit

digitizing level data that is utilized as input to the texture analysis (PCI Geomatics, 2009), it was necessary to convert images from amplitude to a digital number. All radar images were rescaled from their original 32-bit to an 8-bit quantization level. During this process, the image values were converted using the minimum and maximum backscatter values calculated from the image histograms. A linear function was applied to evenly scale the data values from the input range (minimum and maximum values) to an output range of 0 to 255. The histogram of each radar image was considered individually, as the images were taken using different radar specifications and would not be expected to possess the same range of backscatter values. In Figure 4.2 the R-1 standard mode 7 (S7), 2008 image was rescaled from its 32-bit amplitude values to an 8-bit digital number image. This transformation reclassified the range and unit that were represented by each pixel, and maintains a comparable coefficient of variation (CV).

Work by Amaral *et al.* (1997) demonstrates that forest clearing and forested area can be discriminated based on the spatial contiguity within R-1 F2 and F5 images 32-bit and 8-bit magnitude image. In this study, lower radiometric resolution and geometrically degraded images (resampling resolution of 12.5 m) did not affect the discrimination of classes based on the range value of the semivariogram. The results show that the 8-bit rescaled images did maintain texture content for the discrimination of forest and non-forest land cover types.
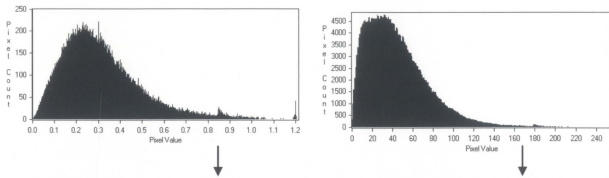
| Statistics | Input amplitude values | Rescaled brightness values |
|---|---|---|
| Mean | 0.198 | 44.81 |
| Standard deviation | 0.151 | 29.64 |
| CV | 0.611 | 0.661 |

Figure 4.2: Histogram and statistics of the R-1, S-7 2008 original image (left) and rescaled (right) images.

## 4.2 Image investigation

The outcomes of this study rely on two main assumptions. The first is that the NDVI imagery is a reliable representation of the land cover types that represent the TTI within the study area, and the second is that land cover information cannot be extracted directly from the original radar backscatter image.

An initial backscatter signature set for tundra and taiga land cover types is utilized in order to investigate the hypothesis that raw backscatter is too wrought with high frequency noise to be useful for characterizing differences between the two environments. This analysis is completed by considering descriptive statistics including mean, standard deviation, range, and kurtosis as well as identifying the class overlap between tundra and taiga land cover. If the descriptive statistics are similar, then the initial assertion is correct, and further investigations of ways to increase the land cover class separation are required.

The accuracy of the NDVI images is examined to ensure that they are suitable as a baseline representation of the vegetation. For each NDVI image, the accuracy is calculated by recording the ratio between correct and incorrect image pixels as identified from the field data.

Variograms are used to gain a sense of the spatial distribution of tundra and taiga land covers. To facilitate an investigation of the variogram parameters, two 600x600 m areas, one representing forest and one representing non-forest land cover were extracted from each R-1 image. The data were exported as an $x$, $y$ and $z$ table where $x$ and $y$ represent the geographic coordinates and z is the backscatter value at that location. The $x$, $y$ and $z$ data are analyzed to create a semi-variogram and to apply a variogram model to the data. Two components of the variogram are considered, those being the range and the nugget. Figure 4.3 provides an example of how these parameters are obtained from the variogram.
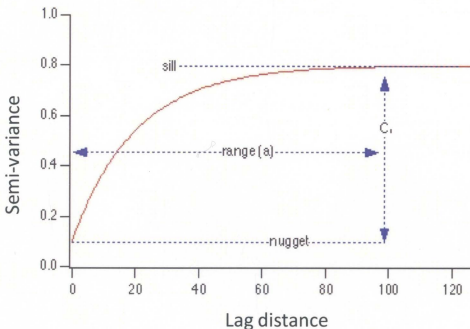


Adapted from Babish, 2006.

Figure 4.3: Components of a variogram.

The range is the distance at which the semi variance begins to plateau and will be used to indicate the distance at which there is minimal spatial autocorrelation between the image pixels (Babish, 2006). Conceptually, this range is also the optimal size window needed to capture the spatial relationships of pixel values that exist within each land cover class. The nugget value is the amount of semi-variance that exists between two neighbouring pixels (i.e. at lag 1). This value can provide information on the amount of noise that exists locally in a radar image.

The results of the variogram analysis were used in two ways. Firstly, the nugget values provided an indication of the magnitude of high-frequency noise that is present in the radar imagery. Secondly, the range values complemented the search for an optimal texture measures filter size, which will help identify the separation between forest and non-forest land cover types and also at what filter size(s) there is the highest correlation with the NDVI.

## 4.3 Texture analysis

First order texture measures emphasize the spatial relationships regarding brightness values in an image. The types of filters that are useful in order to enhance the separability of forested and non-forested land cover within the TTI environment were selected because of the successes from previous studies (See Section 2.4.2) and on the mathematical framework that is expected to be produced by a particular texture measure. The first order texture measures that were selected included: coefficient of variation, energy, entropy, kurtosis, mean, skewness and variance. A brief explanation of each of

these texture measures along with their respective equations is presented in Appendix B.1.

Second order texture measures emphasize the spatial arrangement of pixels within an image including the size, shape and pattern. These texture measures are based on a grey level co-occurrence matrix (GLCM) which is a tabulation of how often different combinations of grey levels occur in an image, and its calculation is based on the relationship of one pixel to a nearby pixel, referred to as the reference pixel and the neighbour pixel, respectively. Relationships expressed in the GLCM are calculated in one of eight possible directions: north, south, east, west, northeast, northwest, southeast and southwest. For this study, the Arctic tree line is assumed to have the same probability of occurring in all directions (i.e. is isotrophic), and so all directions are considered equally during analysis. The immediate neighbour pixel (lag=1) was used in all calculations of second order texture measures. Second order texture measures selected on the criteria outlined in the above section include: contrast, correlation, dissimilarity, entropy, homogeneity, inverse difference and mean. An explanation of each of these texture measures along with their respective equations can be found in Appendix B.2.

The radar images are clipped to correspond with an area that is 1 km greater than the 8x8 km study area extent. This decreases image processing time and facilitates data continuity. The sub-region area is larger than the actual extent of the study area to eliminate data loss at the border during texture analysis. Since texture is calculated using *n x n* cell filters, values that are ≤ *n-1* pixel from the image border will return an invalid filter output calculation due to missing data. Creating a 1 km 'buffer zone' eliminates this

problem by allowing the filter function to use data just outside the study area, up to *n-1* pixel away.

## 4.4 Product development

The development of an R-2 vegetation product is the main objective of this study. This objective is accomplished through two phases. Phase one completes an investigation of R-1 images only, identifying through different methods which texture measure and window size best help to delineate between tundra and taiga and produce a high correlation with the matching NDVI image. Phase two is an examination of R-2 images only. The R-2 images are analyzed following the most effective procedure as identified through phase one.

### *4.4.1 Texture measure selection phase*

Applying every texture measure to all radar imagery on a 'trial and error' basis would have been very inefficient. Instead, a more practical approach was taken. Through an investigation of past research (Dekker, 2003; Haack, 2007; Kurvonen and Hallikainen, 1999; Luckman *et al.*, 1997; Ulaby *et al.*, 1986) and the mathematical processes taking place in order to calculate a given texture measure, a preliminary list was created of suitable texture measures. This list contains texture measures that were successfully applied in previous SAR studies or were mathematically justifiable to be used given the radar data that were available. Both first and second order texture measures were included in this list.

A range of window sizes was tested for each texture measure. The sizes differ between first and second order texture analysis because a larger window size is required for second order analysis to allow for calculation of the GLCM. For first order texture analysis of the standard mode images, filter sizes ranging from 5x5 to 25x25 cells were assessed, corresponding to ground measurements of 150x150 m to 750x750 m, respectively. The second order texture measures applied to the standard mode images used filter sizes from 15x15 to 53x53 cells, or 450x450 m to 1590x1590 m, respectively.

In terms of first order texture analysis for fine mode imagery, filter sizes ranging from 3x3 to 45x45 cells were investigated for areas ranging from 27x27 m to 405x405 m. Smaller filter sizes were considered for the texture analysis of the fine mode image in order to see if filters that represent a smaller spatial area could capture information about tree islands, which are usually smaller than 30x30 m and cannot be characterized using the standard mode images. For second order texture analysis of the fine mode images, filter sizes of 45x45 to 91x91 cells, or 405x405 m to 819x819 m were used. The mean and standard deviation statistics across each texture image for tundra and taiga land cover were compared to the results of the variogram analysis to determine if they produced similar results. Selected optimal texture filter sizes are based on these criteria.

Once the appropriate texture measures and window sizes were identified and the optimal window size selected, the analysis was applied to all remaining Radarsat-1 (R-1) SAR images. The texture images were then considered potential radar-derived vegetation variables and were subject to another separability analysis to determine whether texture analysis improved class separability when compared to the backscatter analysis results alone. The filtering function used to produce the optimal R-1 vegetation product was

applied to all R-2 images in order to implement the R-2 product development phase of this project.

A dataset of 77 field observation points (36 forest and 41 non-forest) was extracted from the second set of field points in order to establish which of the first and second order texture measures increased the amount of information contained within and about forested and non-forested land cover. The pixel information contained at the location of the field point was extracted from each texture measure output image and the statistical difference between forested and non-forested land cover is explored using the Kolmogorov-Smirnov (KS) test (Burt and Barber, 1996). The KS test determines if two data sets differ significantly by comparing the cumulative distribution of two different samples. The null-hypothesis ($H_0$) for this test with respect to the thesis research, was that the sample distributions for forest and non-forest land cover were equal (i.e. possess the same descriptive statistics). Using a confidence interval of 95%, $H_0$ was rejected if the probability was greater than 0.05, indicating that the two land cover types were most likely to come from different distributions. If the forest and non-forest distributions are from different populations, this means that each class has a particular set of radar backscatter values that statistically defines them.

A variogram analysis was utilized with the R-2 images to define the distance at which spatial autocorrelation becomes random, or negative, indicating an optimal window size. The results of the variogram analysis were supported through further analysis, which have seen a reoccurrence of the filter sizes indicated by the variogram, thus verifying the optimum window size.

The size and type of filters that were carried forward and applied to R-2 images were isolated based on two criteria, which had to occur together: there was a significant difference between forest and non-forest land cover demonstrated through the K-S test and there was a significant correlation of the R-2 filtered image with the nearest anniversary date NDVI image.

### 4.4.2 Application phase

The 2008 NDVI image is used as a reference image in order to assess the optimal R-2 image mode for delineation between the tundra and taiga land cover types. The examination of R-2 data introduces a new ultra-fine data mode, having a nominal spatial resolution of 3 m. When applying texture measures, filter sizes corresponding to the spatial area appropriate to fine and standard mode data are applied. However, smaller filter sizes are examined to see if higher resolution data can be used to capture information about tree islands, while still creating enough class separation to statistically distinguish between tundra and taiga land cover. An investigation of the results of the K-S test and the correlation coefficients are carried out with respect to the R-2 images to determine which R-2 mode is most appropriate for delineating forest and non-forest land cover.

### 4.5 Results evaluation

Due to different look angles and the relationship to the topography of the signal recorded at the sensor, it is hypothesized that the R-2 derived product will moderately correlate with the NDVI image. An independent set of field data points is applied using

the same set of procedures to assess the accuracy of the final vegetation product. During this evaluation, the final radar-derived vegetation variable is investigated in terms of its ability to identify the TTI compared to a raw backscatter image. This is accomplished by creating a profile that represents a transect across the TTI. The texture-transformed radar image is anticipated to differentiate forest from the non-forest land cover types, however, the analysis outputs are further analyzed to identify possible sources of errors as they relate to landscape parameters of slope, elevation and aspect.

## 5.0 Introduction

The results are organized such that data processing is presented first, followed by texture analysis. Texture analysis is the main focus of this research and contains results for the R-1 based texture measure selection stage, as well as the R-2 texture measure application phase.

## 5.1 Data processing

Data processing was completed in order to prepare the images for analysis. Data processing comprises image pre-processing and image investigation. Image pre-processing employed a georectification of all images. For image investigation, an exploration of the accuracy and class separability of the NDVI was performed as well as an investigation of the effects of moisture on the radar backscattering. Furthermore, a variogram analysis was performed on the R-1 dataset to identify the spatial dependence of backscattering values.

### 5.1.1 Geometric correction

The RMS error indicates how much the corrected image deviates from selected ground control points, which relate to a map projection for UTM zone 21 row U. The RMS error is represented in both pixels and metres where the RMS in metres is calculated by multiplying the RMS per pixel by the spatial resolution corresponding to the standard (25 m), fine (9 m) and ultrafine (3 m) image mode (Table 5.1). RMS errors

for standard mode images range from ±0.42 to ±0.97 pixels, or ±10.5 m to ± 29.1 m, respectively. For fine mode images, the lowest RMS is ±0.22 pixels (±2.0 m) and the highest is ±1.26 pixels (±11.5 m), while for ultrafine mode images the RMS is between ±0.34 (±1.02 m) and ±3.07 pixels (±9.21 m). During the texture measure selection phase of the thesis, the size of the smallest texture window for standard and fine mode images is 150x150 m (5x5 cells) and 27x27 m (3x3 cells), respectively. The geographical extent of these window sizes is greater than the RMS error and therefore does not significantly affect the spatial congruence of the radar image set.

Table 5.1: Root mean square (RMS) error of geometrically rectified images.

| Image Mode | RMS (± pixel) | RMS (± metre) | Date |
|---|---|---|---|
| F1 | 0.22 | 2.00 | 9/26/2005 |
| F2 | 0.88 | 8.80 | 8/27/2009 |
| F4 | 0.51 | 4.60 | 9/13/2009 |
| F5 | 0.41 | 3.69 | 9/7/2009 |
| F21F | 1.26 | 11.30 | 9/3/2009 |
| FQ19 | 0.68 | 6.10 | 9/17/2009 |
| S1 | 0.93 | 23.25 | 8/7/2001 |
| S3 | 0.79 | 18.17 | 9/10/2009 |
| S4 | 0.89 | 22.25 | 9/10/2009 |
| S5 | 0.63 | 15.75 | 8/3/2008 |
| S6 | 0.58 | 14.50 | 9/24/2009 |
| S7 | 0.42 | 10.50 | 9/7/2008 |
| S7 | 0.49 | 12.25 | 9/6/2009 |
| SQ21 | 0.97 | 29.10 | 9/20/2009 |
| U2 | 3.07 | 9.21 | 9/3/2009 |
| U17 | 1.06 | 3.18 | 8/31/2009 |
| U27 | 0.34 | 1.02 | 8/21/2009 |
| U27 | 0.34 | 1.02 | 9/14/2009 |

## 5.1.2 Exploratory data analysis

An exploration of the data will provide insight to the image characteristics in relation to the spatial variability of forest and non-forest land cover. This exploration is undertaken for the R-1 and NDVI datasets.

### 5.1.2.1 Radar Backscatter

Initial investigations of the R-1 images show that forest and non-forest land cover is not statistically separable when using the raw backscatter image values. This trend can be seen in Table 5.2, which shows the mean and $\pm 1.5$ standard deviations (SD) for each of the R-1 images for forest and non-forest land cover. The statistics help to gain a perspective on the spread, as well as the overlap of radar brightness values for forest and non-forest land cover, where the mean $\pm 1.5$ SD is inclusive of 82% of the data contained in each class. The mean brightness values for forested land cover are between 56.15 and 42.97, and those for non-forest land cover, range from 51.41 to 37.84. The overlap that exists for forest and non-forest land cover means that their distributions are similar, and would not be able to be delineated based on only the raw backscatter information. Class over-lap between forest and non-forest land cover is shown for each image in Figure 5.1. This figure indicates that the backscatter values that represent forest and non-forest are highly variable, rendering the raw backscatter image not suitable for land cover classification.

Table 5.2: Forest and non-forest mean and standard deviation brightness value for R-1 images.

| | Forest | | Non-forest | |
|---|---|---|---|---|
| | Mean | +/- 1.5 SD | mean | +/- 1.5 SD |
| 2001 (S1) | 43.75 | 29.58 | 38.17 | 31.97 |
| 2005 (F1) | 53.51 | 32.95 | 56.03 | 42.88 |
| 2008 (S5) | 42.97 | 24.93 | 44.43 | 29.23 |
| 2008 (S7) | 56.15 | 32.48 | 51.41 | 34.64 |
| 2009 (S4) | 47.76 | 28.89 | 37.84 | 24.60 |
| 2009 (F3N) | 48.52 | 31.56 | 47.47 | 35.28 |
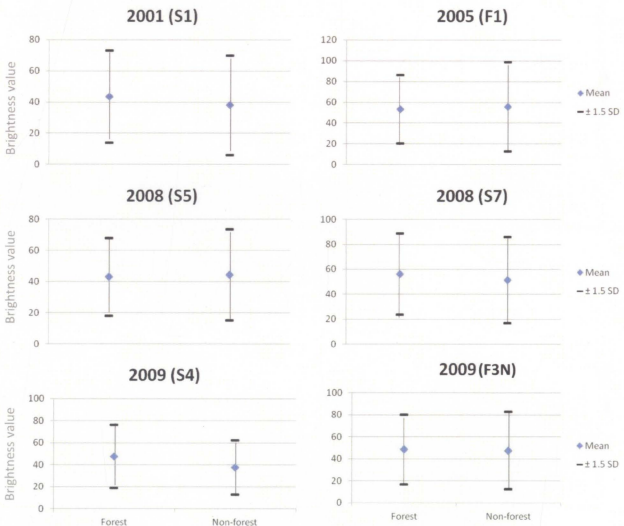


Figure 5.1: Forest and non-forest mean and standard deviation brightness value plot for R-1 images.

*5.1.2.2 NDVI*

An error matrix (or contingency table) provides an evaluation of how well the NDVI imagery is representative of the field data. In order to create an error matrix, the NDVI images are classified by creating a threshold NDVI value using the tree height information contained in the field data, as well as the minimum, maximum and mean NDVI values which are representative of forest and non-forest land cover (See Table 5.3). Mean and standard deviation for forest land cover in the 2001, 2005 and 2008 NDVI images is $0.55 \pm 0.11$, $0.64 \pm 0.12$ and $0.67 \pm 0.09$, respectively. Correspondingly, for non-forest land cover in the 2001, 2005 and 2008 NDVI images the mean and standard deviation is $0.44 \pm 0.10$, $0.49 \pm 0.10$ and $0.55 \pm 0.10$. These statistics indicate that the distribution of NDVI values that represent forest and non-forest are separable. This class separation can be seen for the 2005 NDVI image in Figure 5.3. The statistics extracted for forest and non-forest from the NDVI were utilized to set a threshold value for forest of 0.6, which will be used for differentiating between the forest and non-forest land cover. Although there is a slight overlap in the spread of NDVI values for forest and non-forest (Figure 5.3), it was found through the field data that these are areas of vegetation cover that have a high NDVI value (i.e. strong chlorophyll content), but do not meet the height requirements in order to be classified as strictly forest. A similar method was shown to be useful in Evrendilek and Gulbeyaz (2008) for NDVI classification of Mediterranean type forests. Images are classified such that NDVI = -1 to 0.6 represents non-forest and NDVI = 0.6 to 1 represents forest. The classified NDVI image from 2008 is presented in Figure 5.2. This figure also highlights the location of the 36 forest and 41 non-forest field points in the reference dataset.
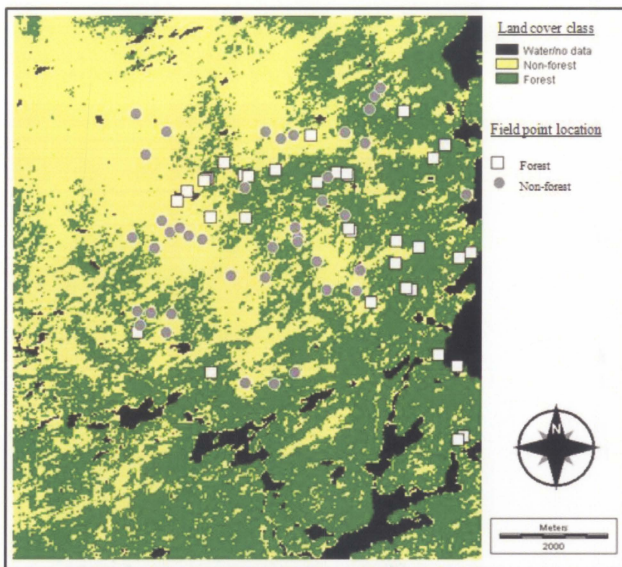
Figure 5.2: Forest and non-forest classification of 2008 NDVI with locations of reference field points.

Table 5.3: Descriptive statistics for 2001, 2005 and 2008 NDVI images for forest and non-forest classes.

| Image | NDVI 2001 | | NDVI 2005 | | NDVI 2008 | |
|---|---|---|---|---|---|---|
| Land cover | Forest | Non-forest | Forest | Non-forest | Forest | Non-forest |
| Range | 0.46 | 0.49 | 0.43 | 0.39 | 0.36 | 0.36 |
| Maximum | 0.73 | 0.64 | 0.81 | 0.58 | 0.81 | 0.59 |
| Minimum | 0.28 | 0.15 | 0.38 | 0.28 | 0.45 | 0.41 |
| Mean | 0.55 | 0.44 | 0.64 | 0.49 | 0.67 | 0.55 |
| ±1.5 SD | 0.11 | 0.10 | 0.12 | 0.10 | 0.09 | 0.10 |
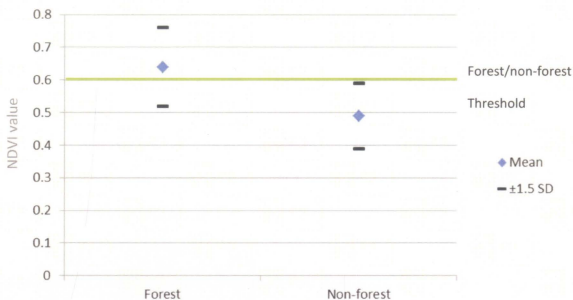
Figure 5.3: Descriptive statistics plot showing forest and non-forest land cover classes for 2005 NDVI image

The error matrix created using the land cover data from the reference field points and the classified 2008 NDVI, reports that the user's accuracy for forest and non-forest land cover is 86.8% and 92.3% respectively, with an overall accuracy of 89.6%. The producer's accuracy for forest and non-forest land cover is 91.6% and 87.8% respectively (Table 5.4). Correspondingly, Tables 5.5 and 5.6 contain the error matrix for the 2005 and 2001 NDVI images. All NDVI representations of forest and non-forest classes have accuracies of above 83%.

Table 5.4: Error matrix for 2008 NDVI.

| Reference data | 2008 NDVI | | | | |
|---|---|---|---|---|---|
| | Forest | Non-forest | Total | PA (%) | EO (%) |
| Forest | 33 | 3 | 36 | 91.7 | 8.3 |
| Non-forest | 5 | 36 | 41 | 87.8 | 12.2 |
| Total | 38 | 39 | 77 | | |
| UA (%) | 86.8 | 92.3 | | | |
| EC (%) | 13.2 | 7.6 | | | |
| OA | | | | | 89.6% |

Abbreviations: PA= producer's accuracy, EO= error of omission, UA= user's accuracy, EC=error of commission, OA= overall accuracy.

Table 5.5: Error matrix for 2005 NDVI.

| Reference data | 2005 NDVI | | | | |
|---|---|---|---|---|---|
| | Forest | Non-forest | Total | PA (%) | EO (%) |
| Forest | 34 | 2 | 36 | 94.4 | 5.6 |
| Non-forest | 4 | 37 | 41 | 90.2 | 9.8 |
| Total | 38 | 39 | 77 | | |
| UA (%) | 89.5 | 94.8 | | | |
| EC (%) | 10.5 | 5.2 | | | |
| OA | | | | | 92.2% |

Abbreviations: PA= producer's accuracy, EO= error of omission, UA= user's accuracy, EC=error of commission, OA= overall accuracy.

Table 5.6: Error matrix for 2001 NDVI.

| Reference data | 2001 NDVI | | | | |
|---|---|---|---|---|---|
| | Forest | Non-forest | Total | PA (%) | EO (%) |
| Forest | 30 | 6 | 36 | 83.3 | 16.7 |
| Non-forest | 7 | 34 | 41 | 85.4 | 14.6 |
| Total | 37 | 40 | 77 | | |
| UA (%) | 81.1 | 85.0 | | | |
| EC (%) | 18.9 | 15.0 | | | |
| OA | | | | | 83.1% |

Abbreviations: PA= producer's accuracy, EO= error of omission, UA= user's accuracy, EC=error of commission, OA= overall accuracy.

A change in biomass over time may have caused the classification accuracy to be a little lower with the 2001 NDVI classification. This trend can be seen in the NDVI statistics, where the mean NDVI values for forest (2001=0.55; 2005=0.64; 2008=0.67) and non-forest (2001=0.44; 2005= 0.49; 2008=0.55) increase over the seven year time period. The trend, however, is not shown in the accuracy assessment matrices, as for all three classifications, although they are not statistically significant, the error of commission of forest is the highest. This type of error reports on the proportion of the forest NDVI class that 'includes' field observed non-forest points. Had the increase of NDVI over time caused an error on the 2001 or 2005 image classifications (non-forest NDVI vs. 2008 forest field data), it would have been read through the commission error of the non-forest class and would have emphasized this error over the omission error, which is not the case. The proportions of omission and commission error are relatively balanced (i.e. about the same) and they are non-significant for all three classifications. This means that the errors can be attributed to overlap of outlying values (high-end-of-range low-NDVI in forest class and low-end-of-range high-NDVI in non-forest class). Also, some of the error can be attributed to the discrepancy of size of the field data sampled area (1x1 m quadrants) and the image pixel resolution (30x30 m).

A two-sample Kolmogorov-Smirnov (KS) test (Burt and Barber, 1996) between the NDVI values represented by forest and non-forest reference points revealed a significant separability between forest and non-forest land cover types in the NDVI. The two-sample KS test identifies whether the cumulative distributions of two samples are similar. The null hypothesis ($H_0$) is that two samples come from the same distribution. Using a confidence interval of 95%, $H_0$ is rejected if $\alpha \leq 0.05$, thus indicating that the two

data samples come from different distributions. For the 2001 NDVI, the KS value calculated between forest and non-forest land cover is 1.708 with α=0.006. For the 2005 and 2008 NDVI, the KS statistics is 2.340 and 2.077, respectively, both with α=0.000 (Table 5.7). These results demonstrate that forest and non-forest land cover come from distributions that are statistically different, and therefore can be distinguished from one another when classified based on the 0.6-NDVI threshold value.

Table 5.7: Results of two sample Kolmogorov-Smirnov (KS) test for NDVI classified images (α=0.05).

| | NDVI 2001 | NDVI 2005 | NDVI 2008 | |
|---|---|---|---|---|
| KS | 1.708 | 2.340 | 2.077 | $\alpha = 0.05$ |
| $\alpha_{KS}$ | 0.006 | 0.000 | 0.000 | |

Results from the contingency table and the two-sample KS test establish the NDVI images as a suitable reference image by which to measure and test the accuracy of radar-derived vegetation products.

### 5.1.3 Moisture effects

The radar backscatter is positively related to the amount of moisture in a target object, thus, as moisture content increases, so does the brightness value on a radar image (Ulaby and El-Rayes, 1987). The R-1 and R-2 images were acquired on days that had followed varying amounts of precipitation, and contain differing amounts of moisture content in objects portrayed on the image. Although this trend cannot be corrected for, it is still a necessary consideration. Due to the image acquisition plan, the effects of moisture on the portrayed radar brightness values cannot be assessed across the entire image set. However, the dataset contains two images with similar specifications; those

being the R-2 S6 mode and the R-1 S5 mode images. The two images are utilized for the investigation of moisture because they have a similar incidence angle (41.70° and 39.24°, respectively) and polarization (both HH) modes (See Tables 3.2 and 3.3 in data section). Where the images do differ is in the amount of precipitation that occurred ten days before and up to the date of acquisition. During this period of time prior to the acquisition of the R-2 S6 and R-1 S5, 95.1 and 20.5 mm of precipitation had been recorded (See Table 3.4 in data section), respectively. All other variables being similar, changes in the brightness values of spatially related pixels may be attributed to a change in moisture content. The backscatter value of forest and non-forest land cover across each image shows that the R-2 S6 image produces higher radar backscatter values for both land cover types when compared to the R-1 S5 image (See Figure 5.4).

These results are expected and demonstrate that for the current datasets, as the moisture content increases, so do the radar brightness values for both the forest and non-forest environments. Statistics of the forest and non-forest field point sample are presented in Table 5.8. Note that the backscatter values for the image with more moisture content (R-2 S6) are more variable. This suggests that in such conditions, the differentiation of forest and non-forest classes, based on the raw backscattering, is more difficult.
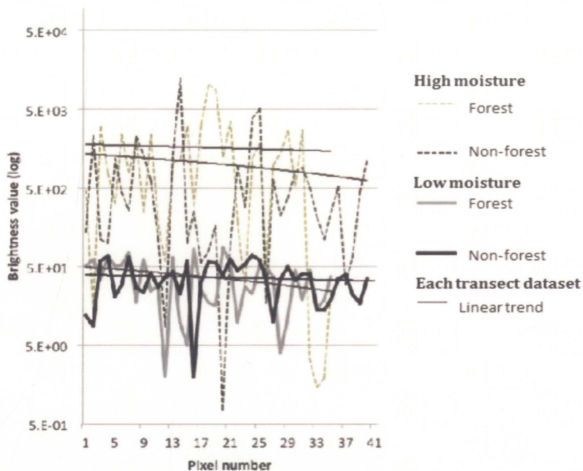
Figure 5.4: Backscatter response (in $\beta_0$) of forest and non-forest land cover for low (R-1 S5) and high (R-2 S6) moisture conditions.

Table 5.8: Brightness value (in $\beta_0$) statistics for forest and non-forest field points with low and high moisture.

| Moisture conditions | Low | | High | |
|---|---|---|---|---|
| Image | R-1 S5 | | R-2 S6 | |
| Land cover | Forest | Non-forest | Forest | Non-forest |
| Mean | 37.40 | 36.80 | 1643.88 | 989.83 |
| Standard deviation | 24.30 | 18.26 | 2300.95 | 2110.98 |
| Coefficient of variation | 0.65 | 0.50 | 1.40 | 2.13 |

### 5.1.4 Variogram

For all images, except the R-1 2008 S5 mode, the variogram derived range value is higher for non-forest than it is for forest land cover (Table 5.9). Variogram analysis

does not include the 2009 S4 and 2009 F3N R-1 images, as these images have a matching date R-2 image and are utilized later in the methodology for comparison of R-1 to R-2 radar derived vegetation products. The range is indicative of the window size outside which there is the least amount of spatial autocorrelation between pixel backscatter values. Pixels that are nearer to one another than the range value have a lower degree of variability, while those that are further apart than the range have a high degree of variability. A larger window is needed for non-forest than for forest land cover in order to capture the relationship between neighbouring pixels backscatter values. Non-forest is comprised of a greater variation of components (krumholtz, vascular plants, rock, gravel etc.) that are nearer to each other than forest, and so the spatial extent needed to capture the backscatter variation of pixels that represent the land cover is larger.

A high nugget value indicates that there is a large variation among backscatter values. For radar imagery, this is most likely attributed to speckle noise. For forest land cover, the highest nugget value is 737, while the lowest is 324. For non-forest land cover, the highest nugget value is 963 and the lowest is 528. The lowest sill value of the image variograms was 330.17 for non-forest land cover in the 2009 F5 mode image, while the highest sill, 1247.60, was calculated for forest land cover, again for the 2009 F5 mode image. Sill values were measured over the same distance

The correlation coefficient ($R^2$) is a measure of how well the theoretical variogram fits the empirical data. For a variogram fit to be viable, it generally has to have an $R^2 \leq 0.6$ (Babish, 2006). The $R^2$ value for forest land cover (0.448 to 0.946) is always lower than that for non-forest land cover (0.802 to 0.98) (Table 5.9). For forest land cover represented in the 2008 S5 image, the variogram model is only able to account for 44.8%

of the distance based relationship that is occurring in the data. The high nugget value (737) associated with this low correlation value is indicative of high local noise that is found in that data, which cannot be accounted for by the empirical variogram. Thus, the low correlation value and high nugget value for the 2008 S5 image is due to the high amounts of variation in backscatter values of the forest class which causes inconsistencies in the empirical variogram that are not able to be represented by the theoretical model.

Table 5.9: Variogram parameters for forest and non-forest land cover extracted from R-1 images (excluding 2009 R-1 imagery).

| Image ID | Forest | | | | Non-forest | | | |
|----------|--------|------|-------|-------|------------|------|-------|-------|
| | Nugget | Sill | Range | $R^2$ | Nugget | Sill | Range | $R^2$ |
| 2005 F1 | 728 | 771 | 286 | 0.686 | 963 | 1145 | 294 | 0.802 |
| 2001 S1 | 324 | 330 | 372 | 0.946 | 596 | 1248 | 472 | 0.976 |
| 2008 S5 | 737 | 520 | 494 | 0.448 | 720 | 674 | 468 | 0.89 |
| 2008 S7 | 506 | 791 | 348 | 0.725 | 528 | 984 | 472 | 0.98 |

The range value calculated from the variogram analysis suggests the need for a window size which captures ground areas of between 350x350 m and 500x500 m (Table 5.10). For images with a spatial resolution of 30 m these values correspond to a filter window size of between 12x12 and 16x16 cells. The 2001 S1 image has range values for forest and non-forest land cover of 372 m (12x12 cells) and 472 m (16x16 cells). The 2005 F1 image, having the finest spatial resolution, has a variogram range value for forest land cover of 286 m and for non-forest land cover 294 m, both indicating a window size with respect to the image of 29x29 cells. For the 2008 S5 image, the variogram range value for forest is 494 (16x16 cells), and for non-forest 468 (16x16 cells). The 2008 S7 image has a variogram range value for forest and non-forest land cover of

348 (12x12 cells) and 462 (16x16 cells), respectively. The range value is indicative of the distance at which spatial autocorrelation becomes zero or negative. From a variogram point of view, the range is the distance at which the semi-variance plateaus. If the window size of a texture measure exceeds this distance, the brightness values inside the defined window, representing either forest or non-forest, become more heterogeneous, and information about spatial autocorrelation is lost. If the window size of a texture measure is less than the distance of the variogram range value, there is a high amount of noise within the pixels values that represent either forest or non-forest land cover, thus making it difficult to delineate between pixels that belong to the forest class and those that belong to the non-forest class. When these characteristic of the variogram are considered, the variogram range indicates an optimal spatial distance at which to make the window size for texture filters. Only one fine mode image was tested, however, the cell size calculated from the variogram range value is 29x29 cells. For the three standard mode images, the highest calculated variogram range value is 16x16 cells, and the lowest is 12x12cells. The number of texture filter cells ($N_P$), as shown in Table 5.10, is calculated as variogram's range value divided by the image spatial resolution.

Table 5.10: Variogram range value in metre units and corresponding number of pixels (N$_P$) for standard (S1, S5 and S6) and the fine (F1) mode images.

| Image ID | Range (m) | N$_p$ |
|----------|-----------|-------|
| 2001 S1  | 372       | 12    |
|          | 472       | 16    |
| 2005 F1  | 186       | 22    |
|          | 194       | 22    |
| 2008 S5  | 494       | 16    |
|          | 468       | 16    |
| 2008 S7  | 348       | 12    |
|          | 472       | 16    |

## 5.2 Texture analysis

A total of 14 texture measures were applied to the R-1 image set. Two selection criteria were adopted to identify appropriate texture measures to be used with the R-2 dataset. The first criterion was that a texture measure that had been applied to the R-1 had to correlate well with its corresponding date NDVI. The second criterion was that the texture measure had to significantly separate forest and non-forest land cover classes as identified through the field data.

The first criterion was measured using Spearman's correlation rho ($\rho$), a non-parametric bivariate statistic which measures the linear correlation of ranks between two data samples. The statistic $\rho$ ranges from -1.0 to 1.0 where -1.0 denotes a perfect negative relationship and 1.0 indicates a perfect positive linear relationship. Prior to Spearman's correlation being calculated, the sample population was examined for uni-variate and multi-variate outliers for the variables being tested, as these factors are known to affect the results of Spearmans's rank correlation.

The second criterion was measured using a two-sample KS test. The conditions of this test were explained in section 5.1.2.1 and it was applied using the same guidelines to the radar image set. The texture measures were carried through into the R-2 image analysis if they met both criteria in at least one of the R-1 images.

### 5.2.1 Texture measure selection phase (R-1 images only)

In Tables 5.11 and 5.12 Spearman's correlation statistic ($\rho$) and the Kolmogorov-Smirnov $K$ statistic (KS) for first and second-order texture measures, respectively, are displayed. If the result is significant at $\alpha=0.01$ (99% confidence interval) the cell is highlighted in dark grey, while if it is significant at $\alpha=0.05$ (95% confidence interval), the cell is highlighted in light grey. The 2005 F1 and 2009 S4 mode images had significant results for the coefficient of variation texture measure with $\rho=-0.55$; KS=1.09 and $\rho=-0.46$; KS=1.44, respectively. The 2008 S7 image showed significant results for the energy texture measure with $\rho=0.28$, KS= 2.66. No images showed significant results in both statistical tests for the entropy texture measure. The 2005 F1, 2009 F3N and 2009 S4 mode images had significant results for the kurtosis texture measure, having $\rho= -0.31$; KS=2.20, $\rho= -0.50$; KS=1.91 and $\rho= -0.43$; KS=1.78, respectively. Only the 2008 S7 mode image indicated significant results for the mean texture measure, with $\rho= 0.39$; KS=2.54 while only the 2009 S4 mode image showed significant result for the variance texture measure, with $\rho= 0.51$; KS=1.44.

Table 5.11: Correlation and KS test results for first order texture measures applied to R-1 dataset.

| Texture measure | CV | | Energy | | Entropy | | Kurtosis | | Mean | | Skewness | | Variance | |
|---|---|---|---|---|---|---|---|---|---|---|---|---|---|---|
| Image year (mode) | ρ | KS | ρ | KS | ρ | KS | ρ | KS | ρ | KS | ρ | KS | ρ | KS |
| 15 | -0.19 | 1.45 | -0.14 | 1.04 | -0.16 | 0.64 | 0.01 | 1.17 | -0.09 | 1.16 | -0.05 | 1.34 | 0.19 | 1.24 |
| 33 | -0.55 | 1.09 | -0.04 | 2.38 | -0.17 | 1.65 | -0.31 | 2.20 | 0.05 | 2.60 | -0.44 | 1.80 | 0.51 | 1.44 |
| 15 | -0.41 | 0.83 | -0.19 | 0.93 | -0.33 | 0.92 | -0.13 | 1.46 | -0.14 | 0.95 | -0.16 | 1.13 | 0.43 | 0.67 |
| 15 | -0.44 | 0.61 | 0.28 | 2.66 | 0.06 | 2.65 | -0.46 | 1.21 | 0.39 | 2.54 | -0.52 | 1.09 | 0.38 | 0.59 |
| 33 | -0.53 | 0.83 | 0.15 | 2.57 | 0.01 | 2.20 | -0.50 | 1.91 | 0.18 | 2.61 | -0.57 | 1.33 | 0.49 | 0.76 |
| 15 | -0.46 | 1.44 | 0.15 | 1.12 | -0.07 | 0.82 | -0.43 | 1.78 | 0.22 | 0.67 | -0.46 | 1.85 | 0.40 | 1.12 |

Dark Grey: significant at α=0.01 (99% confidence interval); Light grey: significant at α=0.05 (95% confidence interval); White: Non-significant (α is ≥ 0.05).

Table 5.12: Correlation and KS test results for second order texture measures applied to R-1 dataset.

| Texture measure | Contrast | | Correlation | | Dissimilarity | | Entropy | | Homogeneity | | Inverse distance | | Mean | |
|---|---|---|---|---|---|---|---|---|---|---|---|---|---|---|
| Image year (mode) | ρ | KS | ρ | KS | ρ | KS | ρ | KS | ρ | KS | ρ | KS | ρ | KS |
| 2001 (S1) | 0.06 | 1.32 | -0.33 | 1.25 | 0.18 | 1.01 | -0.25 | 0.74 | 0.05 | 1.11 | -0.07 | 0.94 | -0.25 | 0.76 |
| 2005 (F1) | 0.11 | 1.03 | -0.20 | 0.79 | 0.12 | 0.67 | 0.06 | 1.99 | -0.10 | 1.09 | -0.11 | 1.12 | -0.10 | 1.53 |
| 2008 (S5) | -0.18 | 0.48 | -0.03 | 1.00 | -0.14 | 0.89 | -0.18 | 1.29 | 0.07 | 0.69 | 0.07 | 0.91 | -0.16 | 1.13 |
| 2008 (S7) | -0.21 | 1.11 | 0.05 | 0.76 | -0.16 | 0.82 | -0.06 | 1.62 | 0.09 | 0.94 | 0.07 | 0.83 | -0.04 | 1.24 |
| 2009 (F3N) | 0.18 | 1.32 | -0.42 | 1.06 | 0.30 | 1.07 | 0.05 | 1.93 | -0.34 | 0.85 | -0.38 | 0.79 | 0.07 | 1.79 |
| 2009 (S4) | 0.13 | 0.90 | -0.20 | 0.89 | 0.17 | 1.02 | -0.32 | 4.35 | -0.03 | 1.18 | -0.10 | 1.39 | 0.15 | 0.81 |

In Table 5.11, there are 6 of the 7 first order texture measures that show significant results for both criteria in at least one image mode. No second order texture measures met both selection criteria and, as a consequence, they were not applied to the R-2 texture analysis phase. In summary, of the fourteen texture measures, only six met the criteria set for selecting a suitable texture measure, as outlined in Section 5.2, which include first order coefficient of variation, energy, kurtosis, mean, skewness and variance.

The results presented in Tables 5.11 and 5.12 are shown for window sizes of 15 pixels for standard mode imagery and 33 pixels for fine mode imagery. This filter size was determined from the Spearman's correlation and KS criterion results, as well as the parameters from the variogram analysis. Figure 5.5 shows the correlation results for the energy, mean and entropy texture measure for the 2008 S7 mode image at window sizes ranging from 5x5 to 25x25 cells. The highest correlation value with the NDVI is always

for window sizes of 15x15 cells. The same trend is seen in all R-1 texture images which meet both selection criteria. For the fine mode image, the highest correlation is for a window size of 33x33 cells. These results correspond with the maximum window size as identified through the variogram analysis (Section 5.1.4), which indicate a window size for fine mode imagery of 29x29 cell. The window size calculated from the variogram analysis for standard mode imagery suggests an optimal window size between 12x12 cells and 16x16 cells. This implies that an optimal texture measure window size can be reached, which takes into consideration the spatial extent of the tree line and its components.
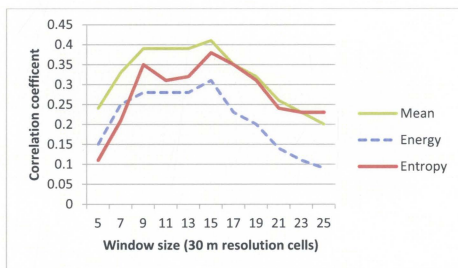


Figure 5.5: Relationship between correlation coefficient and window size of the 30 m spatial resolution standard mode image.

In Wu and North's (2001) study of methods to extract forest cover boundaries from L-band SAR imagery, it was found that the half width of a texture window represents the smallest discernible feature within the filter window. Taking this into consideration, a window size of 15x15 pixels for a standard mode image covers an area

of 450x450 m, meaning that the size of the smallest feature to be detected has a dimension of at least 225x225 m. Field observations indicated that the distance from closed canopy forest to open land cover, transcending the TTI, is between 200 and 600 m. A window size of 15x15 cells is able to capture information within the TTI, yet is large enough to rid of inherent high frequency noise found on the raw radar imagery.

### 5.2.2 Texture application phase (R-2 images only)

An investigation of the R-1 imagery narrowed the pool of texture measures from 14 to 6. The 6 remaining texture measures, which are applied to all R-2 images in this phase include first order coefficient of variation, energy, kurtosis, mean, skewness and variance.

The window size of the texture measures as they were applied to the R-2 imagery was not immediately specified, but rather a range of window sizes were tested. The R-2 dataset has different specifications than the R-1 dataset, and therefore will not have exactly the same spatial extent for spatial autocorrelation among radar backscatter values. The range of window sizes was established from the R-1 analysis (Section 5.2.1). For standard mode imagery (30 m spatial resolution), the window sizes range from 11x11 to 23x23 cells. For fine mode imagery (10 m spatial resolution), the window size ranges from 29x29 to 39x39 cells and for ultra-fine mode imagery (3 m spatial resolution) the window size ranges from 79x79 to 91x91 cells.

The confidence intervals (CI) of the median were calculated as per Equations 5.1 and 5.2 respectively in order identify which of the six texture measures would be most beneficial for characterization of the TTI.

$$\text{Upper CI} = \text{Median} + 1.58 \times (Q3 - Q1)/\sqrt{N} \qquad \text{Equation 5.1}$$

$$\text{Lower CI} = \text{Median} - 1.58 \times (Q3 - Q1)/\sqrt{N} \qquad \text{Equation 5.2}$$

(Tukey, 1977)

where Q1 and Q3 are the values of the 25th and 75th percentile, respectively, as calculated from the quartiles of the dataset. The variable $N$ represents the number of sample values. If the upper and lower confidence intervals of two sample populations do not overlap, then it can be said with 95% confidence that the two samples are from different populations. In the context of this research, the two classes are forest and non-forest land cover. The upper and lower median confidence intervals are shown in Figure 5.6 for each of the six texture measures.

An initial analysis of the texture revealed that the texture measures of coefficient of variation, kurtosis and skewness did not meet both selection criteria when applied to the standard mode and fine mode R-2 imagery. On the right side of Figure 5.6 where the texture measures of coefficient of variation, kurtosis and skewness are displayed, it can be seen that there is no separation between forest and non-forest land cover. This indicates that there is no significant separation between forest and non-forest land cover, and therefore these texture measures would not be useful in rendering a radar-derived product of the TTI.
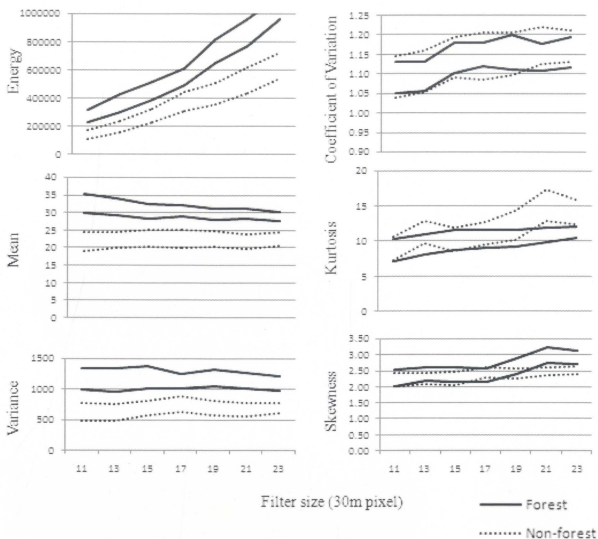
Figure 5.6: Confidence intervals of median for each of the six texture measures identified in the selection phase.

Subsequent to observations made from the median confidence intervals, spearman's correlation results for energy, mean and variance texture measures were calculated (Table 5.13). Spearman's correlation provides a statistical measure of how well the radar-derived product of each texture measures is able to represent the NDVI image, and thus the TTI.

The two highest correlation values were obtained for the VH polarization portion of the fine mode quad-polarized image ($\rho=0.75$) and the fine mode HV polarization image ($\rho=0.66$). Cross-polarized (HV and VH) images show a stronger correlation than

like-polarized (HH and VV) images. In many cases, the results for HV compared to VH polarization are similar. For cases where there is a considerable deviation between the correlation values for HV and VH, such as for the ultra-fine mode mean texture measure (VH=0.35, HV=0.44) and the standard mode variance texture (VH=0.60, HV=0.53), the difference is attributed to the variation in incidence angle (refer to Table 3.2). Only in a few instances were the correlations for like-polarized imagery significant enough to represent a relationship between the texture values and the land cover class. The highest correlations are generally found for the mean texture measure, closely followed by energy then the variance texture measure.

Table 5.13: Spearman's correlation ($\rho$) for all R-2 images.

| Image | | Energy | Mean | Variance |
|---|---|---|---|---|
| | | $\rho$ | $\rho$ | $\rho$ |
| Fine mode | F2 VV | -0.29 | -0.26 | -0.30 |
| | F4 HH | ~ | ~ | ~ |
| | F5 VH | 0.60 | 0.62 | -0.31 |
| | F21HV | 0.62 | 0.66 | 0.60 |
| Standard mode | S3 VV | -0.35 | -0.35 | -0.34 |
| | S6 HH | 0.23 | 0.28 | ~ |
| | S4 VH | 0.60 | 0.62 | 0.60 |
| | S7 HV | 0.55 | 0.57 | 0.53 |
| Ultra-fine mode | U2 VV | ~ | ~ | ~ |
| | U27 HH | 0.24 | 0.30 | 0.20 |
| | U17 VH | 0.32 | 0.35 | 0.31 |
| | U27 HV | 0.37 | 0.44 | 0.34 |
| Standard mode Q | VV | ~ | ~ | ~ |
| | HH | 0.27 | ~ | 0.45 |
| | VH | 0.50 | 0.49 | 0.50 |
| | HV | 0.46 | 0.45 | 0.45 |
| Fine mode Q | HV | 0.47 | 0.51 | 0.44 |
| | HH | -0.21 | ~ | -0.24 |
| | VH | 0.69 | 0.75 | 0.62 |
| | HV | 0.58 | 0.61 | 0.56 |

▨ Denotes significant correlation values at α= 0.001

&ast; Statistics shown in Table 5.13 are for the window size that rendered the most significant correlation. To see the results for all window sizes, please see Appendix C. If there is no data for a given image, this means that it did not meet both criteria (i.e. did not have a significant result for the Spearman's correlation or KS test).

The fine mode quad-polarized image dataset, for which the highest correlation value between the R-1 and the NDVI images was found, integrates four images, each with different polarization, but the same incidence angle. This allows for an assessment of the separation between forest and non-forest land cover with respect to polarization. This relationship is represented using the median confidence interval for the energy (Figure 5.7), mean (Figure 5.8) and variance (Figure 5.9) texture measures at window sizes. The highest class separability is obtained using cross-polarized imagery, with VH polarization indicating slightly more class separation than HV polarization. In all cases, VV polarization displays the least degree of class separation throughout all filter dimensions.
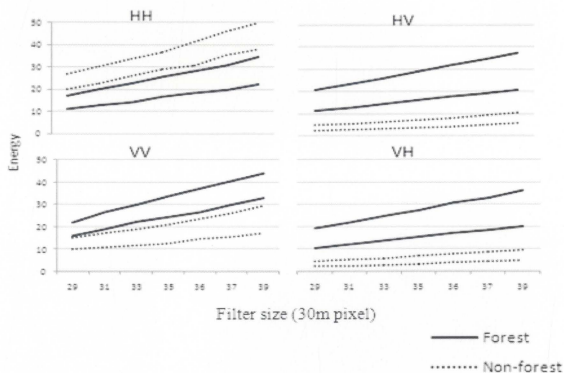


Figure 5.7: Median confidence intervals for forest and non-forest classes when an energy texture measure is applied.
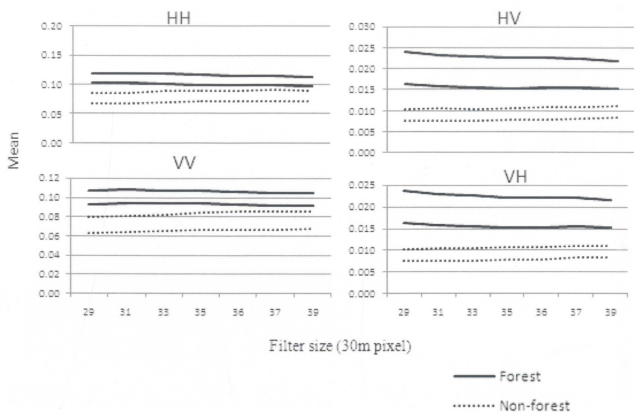
Figure 5.8: Median confidence intervals for forest and non-forest classes when a mean texture measure is applied.
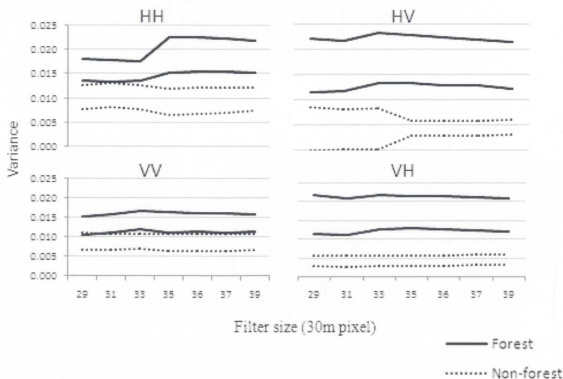


Figure 5.9: Median confidence intervals for forest and non-forest classes when a variance texture measure is applied

# Chapter 6: Discussion

## 6.0 Discussion

The objective of this research was to extract texture information from R-2 SAR images in order to create a radar-derived vegetation product for the TTI. Two criteria of this product are that it correlates well with NDVI and that it is able to distinguish between forest and non-forest land cover types. The results presented demonstrate that the objectives are met. The R-2 product that best represents the TTI environment was derived from a fine mode, VH polarized image transformed using a first order mean texture measure with a window size of 35x35 cells. An evaluation of the derived product and an interpretation of the results with respect to particular radar specifications are presented in this section. These specifications include polarization, orbit, incidence angle and spatial resolution. The effects of window size on the final radar product are also discussed.

## 6.1 Information about the tundra taiga interface

The procedure described above is applied once more using an independent set of field points. After elimination of outliers, the validation set contained 36 forest points and 41 non-forest points. Only the best vegetation product, which is based on the fine mode VH polarized R-2 image was validated, rendering a correlation with the NDVI of $\rho = 0.731$. The correlation from the first analysis using the reference field points was $\rho = 0.750$.

A line transect, when graphed, represents a profile of the behaviour of image pixels over a region of the tundra taiga interface. A profile of the raw SAR imagery

(Figure 6.1) and the radar-derived product (Figure 6.2), respectively, show that a vegetation product using the mean texture measure greatly increases the ability to discern forest and non-forest land cover types. The raw radar brightness values do not indicate that any type of ecosystem transition is present, and the backscatter values for forest and non-forest are undifferentiated. After the image is transformed, a gradual transition zone is revealed between the high second order mean texture values for forest and low values for non-forest. This image also shows that a transition zone between the forest and non-forest land cover can reach a width of 1020 m (34 pixels x 30 m per pixel), by contrast with TTI widths of 200 to 600 m that have been observed in the field. The texture image derived from R-2 imagery help to obtain information about this large-scale characteristic of the TTI that is difficult to measure in the field.
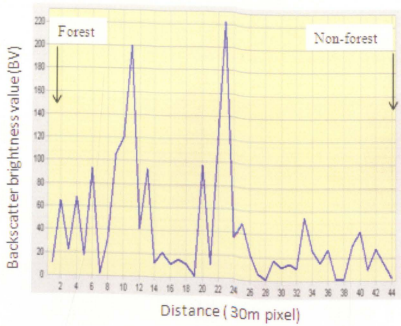
Figure 6.1: Profile across a section of the transition zone for the raw R-2 fine mode VH polarized image. Transition is from forest (left) to non-forest (right).
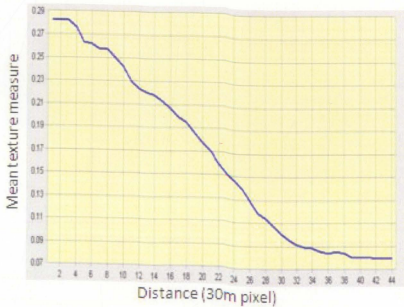


Figure 6.2: Profile across the same section of the transition zone for the transformed fine mode VH polarized image. Transition is from forest (left) to non-forest (right).

A classification of the radar-derived product was created and mapped (Figure 6.3). The thresholds value for classification was selected as the median value of a series of profiles across the transition zone.
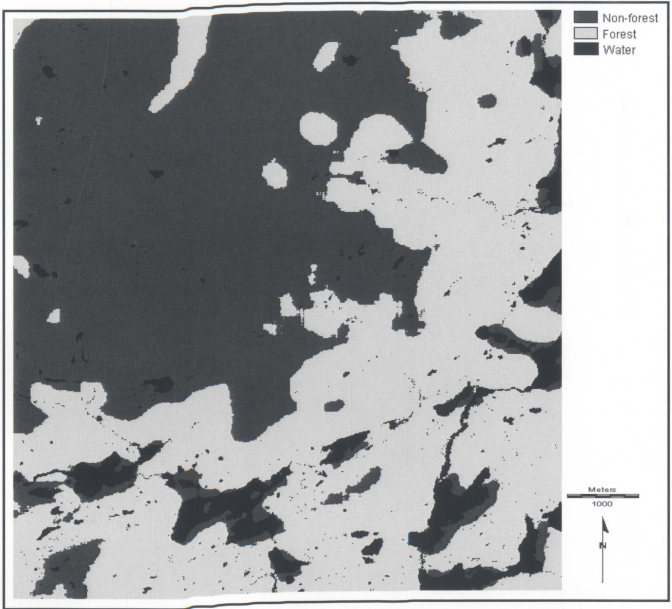


Figure 6.3: Classified radar derived product for the HV portion of the R-2 FQ mode image showing forest and non-forest land cover.

The R-2 derived vegetation product makes it easier to delineate a tree line. For example, consider krumholtz. This land cover includes tree species that are dwarfed or grow horizontally due to environmental limitations. The definition of a tree line for this

research, as adopted from Lescop-Sinclair and Payette (1995), states that a tree line is the northern most position of single-stemmed tree growth forms at least 2.5 m high. On an NDVI, healthy krumholtz having a maximum height of approximately 2 m (LHRG, 2008), are identified as healthy tree species that grow vertically to a height of 2.5 m, because they contain the same amount of chlorophyll. However, the radar product is more representative of the structure and height of vegetation and may exclude krumholtz from being factored as part of the tree line.

A concern of this study, raised by the use of a low-pass texture measure, such as the mean, was that the SAR image transformation may eliminate isolated patches of forest, known as tree islands. However, by looking at the classified radar-derived vegetation product, which is based on a fine mode R-2 image, tree islands are highlighted such that they can be identified. The decision of whether or not to include the tree islands as being part of the tree line is left to the expert users who are still in the process of evaluating the dynamic and ecological significance of these components.

Texture measure filter sizes with dimensions representing ground dimensions of 300x300 m to 450x450 m had the most significant correlation with the NDVI image, and also offered the best separation between forest and non-forest land cover types. These dimensions translate into a filter window size of 15x15 cells for R-2 standard mode images (30 m spatial resolution) and 33x33 cells for R-2 fine mode images (9 m spatial resolution). The initial variogram analysis, as well as the incorporation of window sizes ranging from 50x50 m to 750x750 m in the texture analysis identified the optimal filtering option. A window size of 300x300 m to 450x450 m is also highlighted during the creation of median confidence interval graphs as the highest separation between land

cover types are visible along the x-axis at the filter sizes that correspond to these dimensions.

A window size of 300x300 m to 450x450 m matches well with the spatial extent of the tree line transition environment at the Mealy Mountains site, which, as identified through the field data, can range from 200x200 m to 600x600 m. The process of selecting a texture measure window size as identified in this research provides a more theoretical approach to this task and begins to move away from the arbitrary selections of window size in studies that use radar textures measures, as seen in Luckman *et al.* (1997). As well, instead of having a large range of window sizes to be tested, the amount of analysis that would be required in subsequent studies of the Labrador tree line is narrowed.

## 6.2 Effects of topography

There are some aggregations of pixels on the radar vegetation product which are aberrations. These regions are identifiable using the field data, as well as information from the NDVI. Terrain parameters that may lead to mis-representation of land cover include slope and elevation. Using the digital elevation model, these parameters are calculated, and statistics of the entire study area (SA) are compared to only those identified as misclassified (MC) (Table 6.1). The average slope for the entire study area is 7.5° while the misclassified regions had a mean slope of 20.8°. Looking at elevation, the mean for the entire study area is 616 m, and the mean for misclassified regions is 751 m. Generally, areas of misclassified land cover are located on slopes greater than 19.2° and at elevations greater than 643 m

Table 6.1: Statistics of slope and elevation for the entire study area (SA) and misclassified regions (MC).

|  | SA | MC |  | SA | MC |
|---|---|---|---|---|---|
|  | Slope (°) | Slope (°) |  | Elevation (m) | Elevation (m) |
| Minimum | 2.0 | 19.2 |  | 0 | 643 |
| Maximum | 43.0 | 42.2 |  | 1049 | 1002 |
| Mean | 7.5 | 20.8 |  | 616 | 751 |
| SD | 5.7 | 2.2 |  | 120 | 83 |

The aspect in relation to the incidence angle of the image (38.51°) was also considered and revealed that the misclassified regions are located at orientations which face the platform. This effect causes clusters of high backscatter values to be displayed on the image product, which are confused with the high backscatter values found throughout the forest, and lead to misclassification. If it can be identified which landscape parameters lead to error in the radar product, pixels with these terrain characteristics can be flagged during analysis and assessed when necessary. If considering a time series of radar imagery as a monitoring tool, it would be beneficial with respect to the Labrador terrain to implement a robust radiometric terrain correction as suggested by Small *et al.* (1997).

## 6.3 Radar image specifications

During analyses of the radar imagery, it became apparent that there is a relationship between the strength of correlation with the NDVI and the radar image specifications. Particularly, the specifications are polarization, orbit, incidence angle and spatial resolution. The following section highlights each of these specifications and specifies how they may impact the representation of trees at the TTI.

### 6.3.1 Polarization

Cross-polarized radar data are better at characterizing land cover in the study area, with VH polarization having a higher correlation with the NDVI than HV polarized imagery. The success of cross-polarized R-2 can be attributed to the informaion it provides about volume scattering mechanisms that occur in the tree canopy (Ulaby *et al.*, 1990). The median spread for the fine mode image with a mean texture measure applied (Figure 5.8) indicates that forest and non-forest land cover types are most separable in cross-polarized, and overlap in like-polarized.

R-1 acquires data only in HH polarization, which is not able to support proper detection of land cover at the TTI, as evident in the above results. An improvement of this specification offered by R-2 is the ability to image in all polarization modes (HH, HV, VH and VV). Through this research, cross-polarized SAR information has been proven as a reliable source of data to characterize the TTI. The improvement from R-1 to R-2 of multiple polarization modes means that cross-polarized data are readily available for future monitoring of the TTI.

### 6.3.2 Orbit

More significant correlation results were obtained for imagery recorded from a descending orbit than those from an ascending orbit. This is most likely due to the interaction of radar waves with the terrain. On descending orbit, there is interaction with the trees and vegetation in the valley and along the east side of the mountainous region. The valley is where the majority of vegetation is located, so it is important to have good coverage of this area. On an ascending orbit, there is a high amount of intense backscatter

on the west facing slopes. There is also radar shadow occurring on the side of the mountain facing away from the sensor (backslope).

### 6.3.3 Incidence angle

Figures 6.4 and 6.5 show the level of correlation with the NDVI vs. the incidence angle ($\theta$) for all cross-polarized data. Images with a steep incidence angles (35 to 39º) are better at representing the land cover within the study area than images with a shallow incidence. Verbyla (2001) found that incidence angles between 26 and 31° were most beneficial for detecting the difference between trees during leaf on and leaf off seasons. The study was completed using only R-1 HH imagery. An added benefit of R-2 is that different polarization modes are available. This being the case, the representation of radar backscatter values on an image of the same land cover will be different. The following results provide a guideline as to which incidence angles may be most useful at providing the best radar backscatter separation between tundra and taiga land cover at the tree line. With respect to the study area, the incidence angle combines with the effects of terrain on the radar backscatter by allowing for more interaction with sloping surfaces, thus creating less high frequency noise for images with a steep incidence angle.
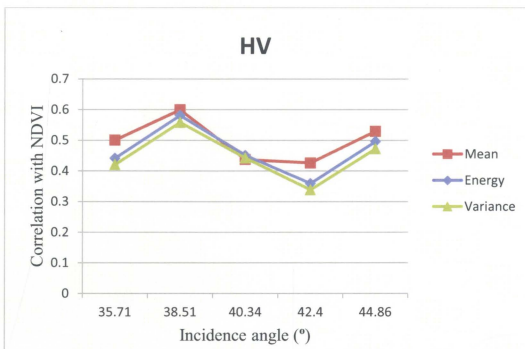
Figure 6.4: Relationship between incidence angle and correlation for R-2 images with HV polarization.
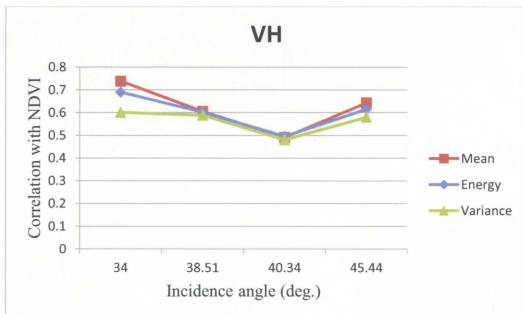


Figure 6.5: Relationship between incidence angle and correlation for R-2 images with VH polarization.

Figure 6.4 indicates that the highest correlation value with NDVI for the HV imagery was recorded with an incidence angle of 38.51°, while for the VH imagery (Figure 6.5), the highest correlation was for an incidence angle of 34.00°. Except for the image in Figure 6.4 with $\theta = 35.71°$, the trend line for correlation and incidence angle has a similar pattern in Figures 6.4 and 6.5. The discrepancy noted at $\theta = 35.71°$ may be attributed to the orbital path, as it is the only image with an ascending orbit.

Although the mean texture measure indicates the highest correlation with the NDVI at almost all incidence angles, the energy and variance texture measures are also very effective at delineating the forest and non-forest classes. When completing analysis of this type, all three texture measures should be equally considered as small variations in image texture may be present in SAR images of locations with slightly different landscape parameters and land cover types.

### 6.3.4 Spatial resolution

The results of this research demonstrate that both standard and fine mode R-2 data are able to characterize the TTI. Masek (2001) and Liu *et al.,* (2005) indicate that higher resolution imagery is more appropriate for delineation of different types of land cover. However, there appears to be a lower limit of approximately 10 m spatial resolution. This emerges from the results of the ultrafine mode R-2 imagery, where only moderate correlations with the NDVI (between 0.20 and 0.44) were obtained (see Table 5.13). An optimal spatial resolution of about 10 m was found for this study area. This finding is also consistent with the findings of Rees (2007), in which images with a spatial resolution of 10 m were shown to produce better class separation between forest and non-forest land

cover. The use of ultra-fine mode R-2 imagery covers a swath width of only about 22 km (CSA, 2008) and would be ineffective to collect data on large areas of the TTI, especially at a circumpolar scale.

Both the standard mode and fine mode radar data provide information about tree cover at the TTI. The use of each of these modes can be tailored to the scale of information that is required. If completing an analysis of the TTI at a continental scale, the swath width and instantaneous field of view of the standard mode imagery is suitable. Fine mode imagery can be used when looking at portions of the transition zone that are narrower or structurally more complex.

# Chapter 7: Conclusion

## 7.0 Conclusion

The use of RADARSAT-2 (R-2) imagery for improved characterization of the tundra taiga interface was investigated in this thesis. An initial texture analysis applied to RADARSAT-1 imagery revealed six potential texture measures that would subsequently be applied to R-2 imagery. Statistical analysis was performed using the Kolmogorov-Smirnov two-sample test, a non-parametric bivariate correlation coefficient and a median confidence interval calculation to reveal which texture measure and corresponding window size performed the best. The optimal texture measure and window size was evaluated based on two criteria. The first criterion was that it significantly separated forest from non-forest land cover, while the second criterion was that the texture measure correlated well with NDVI imagery. These criteria were set in order to accomplish the study's operational and methodological objectives, which are to extract texture information from radar imagery in order to represent vegetation cover, and to create a radar-derived vegetation variable that correlates highly with NDVI images, respectively.

The evaluation of differing polarization modes available from R-2 suggests that vertical-horizontal (VH) polarized imagery best captured the characteristics of the TTI and enhanced the separation between land cover types within the transition zone. The optimal texture measure is first order mean, which outperformed thirteen other measurements. The first order energy texture measure closely matches the results for the mean texture measure and can suitably be used as a proxy texture measure. Future work

should focus on assessing which R-2 incidence angle mode improves the VH and HV polarization radar image derived product.

The conclusions obtained through the research framework of this thesis can be used in several areas of future work. One such area is the application, to a larger scale, of the radar-derived vegetation product. With improved temporal and spatial resolution over multispectral-based NDVI, the R-2 product can be used to monitor the position of the TTI over time.

With additional field data surveys, the product could be adapted to incorporate a greater number of tundra land cover classes, including krumholtz vegetation, to provide a better account of the overall vegetation composition. Dimensions of krumholtz patches and tree islands as well as the gap size between them, are relevant structural information for the interpretation of radar image analysis results. The mean texture radar vegetation product suggests that more land cover types can be imaged, which would lead to a more comprehensive understanding of not only the TTI, but the Arctic ecosystem as a whole.

Particular aspects of this research could be adapted into an automated process for selecting optimal filter window sizes where texture measures are applied. The end user would be provided with spatial statistical information that allow for the selection of a window size that retains spatial dependence and also provides a significant separation between land cover classes that are of interest.

## 8.0 References

Amaral S., Shimabukuro, Y. E., Ahern F. J. and Levesque J. 1997 Pre-processing and semivariogram analysis of Radarsat fine mode images for forest application: Tapajós National Forest, Brazilian Amazon. *Geomatics in the Era of Radarsat 97 Conference*, Ottawa, May 25-30.

Assia, K. and Aichouche, B.-A. (2004) Texture Primitives Description and Segmentation using Variography and Mathematical Morphology. *IEEE International Conference on Systems, Man and Cybernetics*, **7**: 6360-6365.

Babish, G. (2006) *Geostatistics Without Tears*. Environment Canada, Ecological Research Division, Regina.

Bonan, G. B., Chapin, F. S. and Thompson, S. L. (1995) Boreal forest and tundra ecosystems as components of the climate system. *Climate Change*, **29**(2): 145–167.

Burrough , P. A. and McDonell, R. (1998) *Principles of geographical information systems* (Oxford: Oxford University Press).

Burt, J.E. and Barber, G.M (1996) *Elementary Statistics for Geographers,* 3rd Edition. (New York, USA: Guilford Press).

Callaghan, T., Werkman, B. and Crawford, R. (2002) The tundra taiga interface and its dynamics: concepts and applications. *Ambio Special Report,* **12**: 6-14.

Clarke, C., Knight, J. and Gray, J. (2000) Geomorphological reconstruction of the Labrador Sector of the Laurentide Ice Sheet. *Quaternary Science Reviews*, **20**: 1343-1366.

Canadian Space Agency (CSA) (2008) Science and Operational Applications Research for RADARST-2. Retrieved from: http://www.asc-csa.gc.ca/eng/programs/soar/default.asp

Dekker, R. (2003) Texture Analysis and Classification of ERS SAR Images for Map Updating of Urban Areas in the Netherlands. *IEEE Transactions on Geoscience and Remote Sensing,* **41**(9): 1950-1958.

Environment Canada (2010a) National Climate Data and Information Archives: Happy Valley-Goose Bay. Retrieved from: http://www.climate.weatheroffice.gc.ca

Environment Canada (2010b) National Climate Data and Information Archives: Cartwright. Retrieved from: http://www.climate.weatheroffice.gc.ca

Evrendilek, F. and Gulbeyaz, O. (2008) Deriving vegetation dynamics of natural terrestrial ecosystems from MODIS NDVI/EVI data over Turkey. *Sensors* **8**(9), 5270-5302.

Franklin, S., Wulder, M. and Lavigne, B. (1996) Automated derivation of geographic window sizes for remote sensing digital image texture analysis. *Computers & Geosciences*, **22**: 665–673.

Freeman, A. (1998). A three-component scattering model for polarimetric SAR data. *Geoscience and Remote Sensing,* **36** (3):963-973.

Gausman, H. W. (1974). Leaf reflectance of near-infrared. *Photogrammetric Engineering and Remote Sensing,* **40**:183–191.

Getis, A. and Ord, J. K (1992) The analysis of spatial association by use of distance statistics. *Geographical Analysis*, **24**:189-206.

Grace, J., Berninger, F. and Nagy, L. (2002). Impacts of climate change on the tree line. *Annals of Botany*, **90**(4): 537–544.

Grover, K. D. and Quegan, S. (1995) ERS-1 observations and potential for use in tropical forest monitoring. *Quantitative Remote Sensing for Science and Applications,* **2**: 1210-1212.

Guisan, A. and Zimmermann, N. (2000) Predictive habitat distribution models in ecology. *Ecological Modelling,* **135**: 147-186.

Haack, B. (2007) A Comparison of Land Use/Cover Mapping with Varied Radar Incident Angles and Seasons. *Geoscience and Remote Sensing*, **44** (4): 305-319.

Harsch, M., Hulme, P., McGlone, M. and Duncan, R. (2009) Are treelines advancing? A global meta-analysis of treeline response to climate warming. *Ecology Letters,* **12** (10); 1040-1049.

Herold, N., Haack, B., Solomon, E. (2004) An evaluation of radar texture for land use/cover extraction in varied landscapes. *International Journal of Applied Earth Observation and Geoinformation*, **5** (2): 113-128.

Hyyppä, H. and Hyyppä, J. (2001) Effects of stand size on the accuracy of remote sensing-based forest inventory. *IEEE Transactions on Geoscience and Remote Sensing*, **19**(12): 2613-2621.

Jensen, J. (2005) *Introductory Digital Image Processing: A Remote Sensing Perspective*, 3rd Edition. (Upper Saddle River:Pearson).

Jensen, J. (2007) *Remote Sensing of the Environment: An Earth Resource Perspective*, 2nd Edition. (Upper Saddle River:Pearson).

Karl, J. and Maurer, C. (2010) Spatial dependence of predictions from image segmentation: A variogram based method to determine appropriate scales for producing land management information. *Ecological Infomatics*, **5**: 194-202.

Korpela, I., Ørka, H. O., Maltamo, M., Tokola, T. and Hyyppä, J. (2010) Tree species classification using airborne LiDAR – effects of stand and tree parameters, downsizing of training set, intensity normalization, and sensor type. *Silva Fennica,* **44**(2): 319–339.

Kurvonen, L. and Hallikainen, M. (1999) Textural Information of multitemporal ERS-1 and JERS-1 SAR images with applications to land and forest type classification in boreal zone. *IEEE Transactions on Geoscience and Remote Sensing,* **37**(2): 680-689.

LHRG Labrador Highlands Research Group (2008) Field Report 2007. Retrieved from http://www.mun.ca/geog/lhrg/Field_report_2007.php.

Lescop-Sinclair, K. and Payette, S. (1995) Recent advance of the arctic tree line along the eastern coast of Hudson Bay. *Journal of Ecology*, **83**: 929-936.

Liu, Q.-J., Li, X.-R., Ma, Z.-Q. and Takeuchi, N. (2005) Monitoring forest dynamics using satellite imagery - a case study in the natural reserve of Changbai Mountain in China. *Forest Ecology and Management*, **210**: 25-37.

Loehle, C. and LeBlanc, D. (1996) Model-based assessments of climate change effects on forests: a critical review. *Ecological Modeling*, **90**: 1–31.

Luckman, A. J., Frery, A. C., Yanasse, C. and Groom, G. B. (1997) Texture in airborne SAR imagery of tropical forest and its relationship to forest regeneration stage. *International Journal of Remote Sensing*, **18**(6): 1333 -1349.

Lyon, L. G., Yuan, D., Lunetta, R. S. and Elvidge, C. D. (1998) A change detection experiment using vegetation indices. *Photogrammetric Engineering and Remote Sensing*, **64**: 143-150.

Masek, J. (2001) Stability of boreal forest stands during recent climate change: evidence from Landsat satellite imagery. *Journal of Biogeography*, **28**(8), 967-976.

Mather, P. (2004) *Computer processing of Remotely Sensed Images: An Introductions*, 3rd Edition. (West Sussex: John Wiley and Sons Ltd.).

Monsivais-Huertero, A., Chenerie, I., Sarabandi, K., Baup` F. and Mougin, E. (2010) Microwave electromagnetic modeling of Sahelian grassland. *Remote Sensing of Environment*, **31**(7): 1915-1942.

Naesset, E. (1997) Determination of mean tree height of forest stands using airborne laser scanner data. *Journal of Photogrammetry and Remote Sensing*, **52**: 49-56.

PCI Geomatics (2011). Geomatica Version 10.3. Ontario, Canada: PCI Geomatics Enterprises Incorporated.

Payette, S., Fortin, M. and Gamache, I. (2001) The subarctic forest-tundra: the structure of a biome in a changing climate. *BioScience,* **51**: 709–718.

Ranson, K. J, Sun, G., Kharuk, V. I. and Kovacs, K. (2004) Assessing tundra taiga boundary with multi-sensor satellite data. *Remote Sensing of the Environment*, **93**: 283-295.

Rees, W.G. (2007) Characterisation of arctic treelines by LiDAR and multi spectral imagery. *Polar Record,* **43:** 345-352.

Richards, J. (1985) Radar backscatter modelling of forests: a review of current trends. *International Journal of Remote Sensing*, **11**(7): 1299 -1312.

Roberts, B., Simon, N. and Deering, K. (2006) The forests and woodlands of Labrador, Canada: ecology, distribution and management. *Ecological Resources*, **21**: 868-880.

Rouse, J.W., Haas, R., Schell, J. and Deering, D. (1973) Monitoring vegetation systems in the great plains with ERTS. *NASA Special Report*, **351 I**: 309-317.

Santoro, M., Fransson, J., Eriksson, L., Magnusson, M., Ulander, L. and Olsson, H. (2009) Signatures of ALOS PALSAR l-band backscatter in Swedish forest. *IEEE Transaction on Geosciences and Remote Sensing*, **47**(12): 4001-4019.

Schott, J., Salvaggio, C. and Volchok, W. (1988) Radiometric scene normalization using pseudo-invariant features. *Remote Sensing of Environment*, **26**, 1– 16.

Shan, J. and Toth, C. (2009) Topographic Laser Ranging and Scanning: Principles and Processing.Taylor and Francis, Flordia, USA.

Sieber, A. (1985) Forest Signatures in Imaging and Non-Imaging Microwave Scatterometer Data, *ESA Journal*, **9**,431–448.

Skre, O., Baxter, B., Fedorkov, A. and Crawford, R. (2002) How will the taiga-tundra interface respond to climate change? *Ambio Special Report*, **12**: 37-46.

Small, D., Holecz, F., Meier, E., Nuesch, D. and Barmette, A. (1997). Geometric and Radiometric Calibrations of RADARSAT Images. In *Proceedings of Geomatics in an era of RADARSAT*, Ottawa, Canada, May 24-30.

Smith, M., Goodchild, M. and Longley, P. (2007) *Geospatial analysis: A comprehensive guide to principles, techniques and software tools*. (Leicester:Matador).

Tsymbal , O., Lukin , V., Ponomarenko , N., Zelensky , A., Egiazarian , K. and Astola, J. (2005) Three-state locally adaptive texture preserving filter for radar and optical image processing. *Journal on Applied Signal Processing,* 2005:1185-1204.

Tukey, J.W. (1977) *Exploratory Data Analysis*. (Reading, USA:Addison-Wesley).

Ulaby, F., Yate, F., Brisco, B. and Lee, T. (1986) Textural information in SAR images. *IEEE Transactions on Geoscience and Remote Sensing,* **24** (2): 235-245.

Ulaby, F. and El-Rayes. M. (1987) Microwave dielectric spectrum of vegetation Part 11: Dual-Dispersion Model. *IEEE Transaction on Geoscience and Remote Sensing,* **GE-25**: 550-557.

Ulaby, F., Sarabandi, K. , Mcdonald, K., Whitt, M. and Dobson, M.C. (1990) Michigan microwave canopy scattering model. *International Journal of Remote Sensing*, **11** (7): 1223- 1253.

Van der Sanden, J. (2004) Anticipated applications potential of RADARSAT-2 data. *Canadian Journal of Remote Sensing*, **30** (3): 369-379.

Van Leeuwen, M. and Nieuwenhuis, M. (2010) Retrieval of forest structural parameters using LiDAR remote sensing. *European Journal of Forest Research*, **129**: 749-770.

Verbyla, D. L. (2001) A test of detecting spring leaf flush within the Alaskan boreal forest using ERS-2 and Radarsat SAR data. *International Journal of Remote Sensing*, **22** (6): 1159-1165.

Wu, Q. and North, H. (2001) Multi-scale technique for detecting forest boundary from SAR images. *International Journal of Remote Sensing*, **22**(5): 757-772.

**Appendix A: Glossary**

*Backscattering*: the mechanisms by which energy interacts with features on the Earth's surface.

*Kolmogorov-Smirnov (K-S) test*: a non-parametric statistical test that determines if two datasets differ significantly.

*Median*: The numeric centre of a sample. The median separates the higher values of the sample from the lower values.

*Tree island*: individual tree growing at the range edge for that species

*Tundra-taiga interface* or *tree line*: the eco-tone that is characterized as the boundary where the taiga ends and tundra land cover begins.

*Taiga*: a moist sub-arctic environment dominated by conifer land cover.

*Spearman's correlation*: a non-parametric statistical test that measures the statistical dependence between two variables

*Backscatter*: the grey level value found in a radar image which indicates the strength of backscattering that occurs at each pixel.

## Appendix B: Texture measures

The equations for texture measures are taken from the following references: Dekker (2003), Haack (2007), Luckman *et al.* (1997), Kurvonen and Hallikainen (1999), and Ulaby *et al.* (1986).

### B.1: First order texture measures

**Energy**

$$\sum_{i,j} (x_{i,j})^2$$

This measure represents total magnitude of the signal in the window. Due to its large value it may be not suitable for SAR images.

**Entropy**

$$\sum_{i,j} (p_{i,j}) \left( log^2 (p_{i,j}) \right)$$

Where $(p_{i,j}) = \frac{x_{i,j}}{\sum_{i,j}(x_{i,j})}$

Note: if $x_{i,j} <= 0$, its contribution is set to 0.

Entropy is a measure of disorder of the values within the window. It is large for windows with Gaussian (highly disordered) distribution of values, and small for windows with values tightly concentrated around one or several values.

**Kurtosis**

$$\frac{\sum_{i,j}(x_{i,j} - mean)^4}{(M-1)(var)^2}$$

Kurtosis is the fourth standardized moment. This measure describes the degree of peakedness of a distribution. If the distribution has a high and narrow peak, its kurtosis is greater than 3. Gaussian distribution has kurtosis equal to 3. If the peak is broad and flat, the kurtosis is less than 3. Constant-valued windows have kurtosis equal to 0.

## Mean

$$\frac{\sum_{i,j}(x_{i,j})}{M}$$

An arithmetic mean of all values in the texture window.

## Normalized Coefficient of Variation

$$\frac{\sqrt{var}}{mean}$$

A measure of variability of window values, normalized by their mean. This measure is often used in analyzing Synthetic Aperture Radar (SAR) images, as it models statistical properties of SAR speckle.

## Skewness

$$\frac{\sum_{i,j}(x_{i,j} - mean)^3}{(M-1)(var)^{3/2}}$$

Skewness is the third standardized moment. This measure describes the degree of asymmetry of a distribution. If the distribution has a longer left tail, the skewness is negative. Symmetric distributions (including Gaussian and constant) have skewness equal to 0. Otherwise the skewness is positive.

## Variance (*var*)

$$\frac{\sum_{i,j}(x_{i,j} - mean)^2}{M-1}$$

An unbiased estimate of sample variance of values in the texture window.

## B.2: Second order texture measures

**Contrast**

$$\sum_{i,j=0}^{N-1} P_{i,j}(i-j)^2$$

This is the opposite of Homogeneity. It is a measure of the amount of local variation in the image.

**Correlation**

$$\sum_{i,j=0}^{N-1} P_{i,j}\left[\frac{(i-mean_i)(j-mean_j)}{\sqrt{(var_i{}^2)(var_j{}^2)}}\right]$$

Measures the correlation level of neighbouring pixels. When the scale of local texture is much larger than the distance of lag, the correlation texture measure is typically high. When the local texture has a scale similar to or smaller than the lag, there will be low correlation between pairs of pixels apart by the lag distance.

**Dissimilarity**

$$\sum_{i,j=0}^{N-1} P_{i,j}|i-j|$$

Similar to Contrast. High when the local region has a high contrast.

**Entropy**

$$\sum_{i,j=0}^{N-1} P_{i,j}(-lnP_{i,j})$$

Assuming that 0 * ln0 = 0.

Entropy is high when the elements of GLCM have relatively equal values. The entropy measure is low when the elements are close to either 0 or 1 (i.e. when the image is uniform in the window).

## Homogeneity

$$\sum_{i,j=0}^{N-1} \frac{P_{i,j}}{1+(i-j)^2}$$

It is high when GLCM concentrates along the diagonal. This occurs when the image is locally homogeneous in the scale of the length of (SpatPixel, SpatLine).

## Inverse Difference

$$\sum_{i,j=0}^{N-1} \frac{P_{i,j}}{|i-j|^2}$$

Measures image homogeneity. It is high when most of the occurrences in the GLCM are concentrated near the main diagonal.

## Second Order Mean

$$\sum_{i,j=0}^{N-1} i(P_{i,j})$$

Average grey level in the local window

**Appendix C: Spearman's correlation (ρ) and two sample KS test results.**

Cells highlighted in light grey indicate that the value is significant at a 95% confidence level and cells highlighted in dark grey indicate that the value is significant at a 99% confidence interval. Values in **bold** are those used in Table 5.11 and 5.12 of the main thesis.

Table C.1: Spearman's correlation (ρ) and two sample KS test for S3 mode VV image.

| Texture measure | Coefficient of Variation | | Energy | | Kurtosis | | Mean | | Skewness | | Variance | |
|---|---|---|---|---|---|---|---|---|---|---|---|---|
| Filter size | ρ | K-S | ρ | K-S | ρ | K-S | ρ | K-S | ρ | K-S | ρ | K-S |
| 11 | .035 | 1.214 | -.296 | .933 | .074 | 1.478 | -.332 | .812 | .077 | 1.372 | -.272 | 1.232 |
| 13 | -.025 | 1.284 | -.321 | 1.039 | .136 | 1.072 | -.321 | .918 | .117 | .824 | -.297 | 1.251 |
| 15 | -.068 | 1.033 | -.346 | 1.111 | .087 | 1.157 | -.340 | 1.042 | .071 | 1.014 | -.333 | 1.042 |
| 17 | -.090 | .942 | -.340 | 1.075 | .083 | .860 | -.354 | 1.148 | .067 | .824 | -.326 | 1.060 |
| 19 | -.145 | .978 | -.334 | 1.166 | .044 | 1.160 | -.342 | 1.166 | .022 | 1.248 | -.337 | 1.235 |
| 21 | -.149 | .996 | -.333 | 1.269 | .053 | .527 | -.336 | 1.287 | .019 | .633 | -.325 | 1.093 |
| 23 | -.154 | 1.335 | -.325 | 1.254 | -.051 | .636 | -.335 | 1.235 | -.061 | .933 | -.313 | 1.235 |

Table C.2: Spearman's correlation (ρ) and two sample KS test for S4 mode VH image.

| | Coefficient of Variation | | Energy | | Kurtosis | | Mean | | Skewness | | Variance | |
|---|---|---|---|---|---|---|---|---|---|---|---|---|
| Filter size | ρ | K-S | ρ | K-S | ρ | K-S | ρ | K-S | ρ | K-S | ρ | K-S |
| 11 | -.322 | .830 | .566 | 1.992 | -.126 | .669 | .591 | 1.941 | -.145 | .721 | .519 | 2.098 |
| 13 | -.343 | .881 | .575 | 1.675 | -.157 | .860 | .597 | 1.883 | -.188 | .896 | .546 | 1.711 |
| 15 | -.293 | .812 | .602 | 1.729 | -.088 | .651 | .605 | 1.605 | -.115 | .751 | .588 | 1.799 |
| 17 | -.264 | 1.093 | .593 | 1.765 | -.159 | .827 | .611 | 1.711 | -.177 | 1.039 | .595 | 1.765 |
| 19 | -.283 | 1.042 | .581 | 1.765 | -.240 | 1.269 | .609 | 1.641 | -.256 | 1.411 | .569 | 1.659 |
| 21 | -.335 | 1.023 | .575 | 1.447 | -.276 | 1.711 | .611 | 1.547 | -.296 | 1.711 | .564 | 1.550 |
| 23 | -.313 | 1.051 | .596 | 1.671 | -.294 | 1.868 | .616 | 1.547 | -.305 | 1.693 | .561 | 1.532 |

Table C.3: Spearman's correlation (ρ) and two sample KS test for S6 mode HH image.

| Texture measure | Coefficient of Variation | | Energy | | Kurtosis | | Mean | | Skewness | | Variance | |
|---|---|---|---|---|---|---|---|---|---|---|---|---|
| Filter size | ρ | K-S | ρ | K-S | ρ | K-S | ρ | K-S | ρ | K-S | ρ | K-S |
| 11 | -.152 | 1.214 | .226 | 1.781 | -.108 | 1.178 | .279 | 2.098 | .279 | 1.251 | .192 | 1.569 |
| 13 | -.231 | 1.635 | .197 | 1.693 | -.215 | 2.011 | .249 | 2.310 | .249 | 1.781 | .161 | 1.375 |
| 15 | -.126 | 1.030 | .162 | 1.708 | -.070 | 1.426 | .206 | 2.168 | .206 | 1.175 | .155 | 1.744 |
| 17 | -.134 | .993 | .125 | 1.496 | .000 | 1.302 | .201 | 2.011 | .201 | 1.496 | .100 | 1.426 |
| 19 | -.182 | 1.160 | .091 | 1.354 | -.091 | 1.463 | .180 | 1.905 | .180 | 1.354 | .074 | 1.317 |
| 21 | -.159 | .918 | .068 | 1.266 | -.051 | 1.196 | .148 | 1.569 | .148 | 1.266 | .054 | 1.248 |
| 23 | -.142 | .739 | .057 | 1.142 | -.029 | 1.057 | .112 | 1.799 | .112 | 1.142 | .029 | 1.054 |

Table C.4: Spearman's correlation (ρ) and two sample KS test for S7 mode HV image.

| Texture measure | Coefficient of Variation | | Energy | | Kurtosis | | Mean | | Skewness | | Variance | |
|---|---|---|---|---|---|---|---|---|---|---|---|---|
| Filter size | ρ | K-S | ρ | K-S | ρ | K-S | ρ | K-S | ρ | K-S | ρ | K-S |
| 11 | .118 | .787 | .530 | 1.989 | .275 | 1.123 | .524 | 1.777 | .238 | 1.123 | .530 | 1.865 |
| 13 | -.079 | .500 | .506 | 1.883 | .194 | 1.178 | .515 | 1.902 | .098 | 1.017 | .490 | 1.777 |
| 15 | -.122 | .475 | .496 | 1.566 | .201 | 1.211 | .529 | 1.708 | .125 | 1.142 | .472 | 1.584 |
| 17 | -.148 | .578 | .507 | 1.514 | .027 | 1.057 | .544 | 1.729 | -.172 | 1.128 | .488 | 1.478 |
| 19 | -.205 | .539 | .514 | 1.623 | -.063 | 1.302 | .547 | 1.729 | -.060 | 1.335 | .486 | 1.447 |
| 21 | -.207 | .893 | .529 | 1.729 | -.153 | 1.269 | .561 | 1.623 | -.151 | 1.269 | .494 | 1.623 |
| 23 | -.221 | .718 | .550 | 1.517 | -.262 | .736 | .574 | 1.638 | -.247 | .930 | .506 | 1.517 |

Table C.5: Spearman's correlation (ρ) and two sample KS test for F2 mode VV image.

| Texture measure | Coefficient of Variation | | Energy | | Kurtosis | | Mean | | Skewness | | Variance | |
|---|---|---|---|---|---|---|---|---|---|---|---|---|
| Filter size | ρ | K-S | ρ | K-S | ρ | K-S | ρ | K-S | ρ | K-S | ρ | K-S |
| 29 | -.243 | .617 | -.288 | .872 | .240 | .845 | -.260 | 1.222 | .154 | .920 | -.296 | .920 |
| 31 | -.243 | .513 | -.276 | .979 | .269 | .982 | -.253 | .979 | .189 | .842 | -.299 | .964 |
| 33 | -.288 | .893 | -.276 | .857 | .251 | .739 | -.248 | 1.023 | .146 | .920 | -.301 | .842 |
| 35 | -.248 | .786 | -.268 | .875 | .298 | 1.026 | -.244 | 1.023 | .186 | .934 | -.270 | .902 |
| 37 | -.243 | .982 | -.259 | .872 | .281 | 1.071 | -.231 | 1.038 | .181 | .641 | -.273 | .828 |
| 39 | -.244 | .908 | -.261 | .994 | .205 | .534 | -.232 | 1.038 | .095 | .584 | -.278 | .872 |
| 41 | -.240 | .831 | -.267 | 1.009 | .200 | .537 | -.235 | 1.009 | .099 | .626 | -.275 | .825 |

Table C.6: Spearman's correlation (ρ) and two sample KS test for F21 mode HV image.

| Texture measure | Coefficient of Variation | | Energy | | Kurtosis | | Mean | | Skewness | | Variance | |
|---|---|---|---|---|---|---|---|---|---|---|---|---|
| Filter size | ρ | K-S | ρ | K-S | ρ | K-S | ρ | K-S | ρ | K-S | ρ | K-S |
| 29 | -.243 | .670 | .622 | 2.916 | -.171 | .694 | .642 | 2.551 | -.166 | .845 | .591 | 3.008 |
| 31 | -.233 | .532 | .619 | 2.824 | -.177 | .629 | .640 | 2.610 | -.153 | .845 | .597 | 2.946 |
| 33 | -.260 | .940 | .615 | 2.824 | -.217 | .798 | .643 | 2.610 | -.199 | .709 | .597 | 2.946 |
| 35 | -.248 | .786 | .611 | 2.732 | -.271 | .934 | .653 | 2.504 | -.257 | .721 | .602 | 2.824 |
| 37 | -.243 | .918 | .613 | 2.610 | -.269 | .920 | .664 | 2.504 | -.237 | .813 | .599 | 2.717 |
| 39 | -.254 | .908 | .612 | 2.610 | -.270 | 1.023 | .662 | 2.610 | -.247 | .994 | .593 | 2.625 |
| 41 | -.251 | .856 | .608 | 2.717 | -.321 | 1.115 | .652 | 2.610 | -.288 | 1.145 | .582 | 2.946 |

Table C.7: Spearman's correlation (ρ) and two sample KS test for F4 mode HH image.

| Texture measure | Coefficient of Variation | | Energy | | Kurtosis | | Mean | | Skewness | | Variance | |
|---|---|---|---|---|---|---|---|---|---|---|---|---|
| Filter size | ρ | K-S | ρ | K-S | ρ | K-S | ρ | K-S | ρ | K-S | ρ | K-S |
| 29 | -.233 | 1.364 | **.04** | **1.453** | -.013 | .997 | .063 | 1.697 | -.031 | 1.023 | -.009 | 1.222 |
| 31 | -.285 | 1.516 | .03 | 1.302 | -.029 | 1.373 | **.071** | **1.726** | -.070 | 1.329 | -.039 | 1.059 |
| 33 | -.299 | 1.608 | .02 | 1.314 | -.027 | 1.373 | .061 | 1.664 | -.095 | 1.359 | -.035 | 1.195 |
| 35 | -.337 | 1.685 | -.01 | 1.317 | -.062 | 1.679 | .060 | 1.587 | -.144 | 1.649 | -.066 | 1.195 |
| 37 | -.343 | 1.700 | -.01 | 1.210 | -.060 | 1.465 | .052 | 1.679 | -.134 | 1.557 | -.065 | 1.166 |
| 39 | **-.351** | 1.258 | -.02 | 1.302 | **-.078** | **1.634** | .053 | 1.679 | -.152 | 1.726 | -.087 | 1.166 |
| 41 | -.337 | 1.243 | -.05 | 1.267 | -.058 | 1.528 | .046 | 1.451 | **-.156** | 1.542 | **-.104** | **1.145** |

Table C.8: Spearman's correlation (ρ) and two sample KS test for F5 mode VH image.

| | Coefficent of Variation | | Energy | | Kurtosis | | Mean | | Skewness | | Variance | |
|---|---|---|---|---|---|---|---|---|---|---|---|---|
| Filter size | ρ | K-S | ρ | K-S | ρ | K-S | ρ | K-S | ρ | K-S | ρ | K-S |
| 29 | -.496 | 1.332 | -.105 | 1.181 | -.386 | .679 | -.063 | 1.406 | -.358 | .902 | -.309 | 1.235 |
| 31 | **-.509** | **1.498** | -.187 | 1.341 | -.404 | .753 | -.157 | 1.341 | -.364 | .979 | -.283 | 1.199 |
| 33 | -.495 | 1.679 | -.158 | 1.199 | **-.420** | **.952** | -.133 | 1.111 | -.381 | .908 | -.271 | 1.057 |
| 35 | -.505 | 1.818 | -.160 | 1.287 | -.408 | 1.044 | -.136 | 1.145 | -.388 | .985 | -.244 | 1.199 |
| 37 | -.491 | 1.634 | .597 | 1.111 | -.375 | 1.228 | .609 | 1.641 | -.370 | 1.154 | -.305 | 1.005 |
| 39 | -.465 | 1.697 | .599 | 1.005 | -.410 | 1.092 | .611 | 1.547 | -.406 | 1.121 | **-.313** | 1.005 |
| 41 | -.452 | 1.955 | **.604** | **1.217** | -.415 | .970 | **.616** | **1.547** | -.417 | **1.000** | -.313 | 1.005 |

Table C.9: Spearman's correlation (ρ) and two sample KS test for U2 mode VV image.

| Texture measure | Coefficient of Variation | | Energy | | Kurtosis | | Mean | | Skewness | | Variance | |
|---|---|---|---|---|---|---|---|---|---|---|---|---|
| Filter size | ρ | K-S | ρ | K-S | ρ | K-S | ρ | K-S | ρ | K-S | ρ | K-S |
| 79 | -0.29 | 2.31 | 0.00 | 2.05 | 0.00 | 2.60 | -0.05 | 2.49 | -0.03 | 2.58 | -0.09 | 1.85 |
| 81 | **-0.30** | **2.17** | 0.00 | 1.94 | 0.00 | 2.60 | -0.04 | 2.38 | -0.02 | 2.58 | -0.10 | 1.85 |
| 83 | -0.29 | 2.17 | 0.00 | 1.94 | 0.01 | 2.49 | -0.05 | 2.38 | -0.02 | 2.58 | **-0.10** | **1.85** |
| 85 | -0.29 | 2.14 | 0.00 | 1.97 | 0.00 | 2.49 | -0.04 | 2.38 | -0.03 | 2.47 | -0.10 | 1.83 |
| 87 | -0.28 | 2.25 | 0.01 | 1.88 | 0.00 | 2.49 | -0.04 | 2.38 | **-0.02** | **2.60** | -0.11 | 1.85 |
| 89 | -0.27 | 2.35 | 0.02 | 1.95 | 0.01 | 2.49 | **-0.05** | **2.38** | -0.01 | 2.60 | -0.11 | 1.85 |
| 91 | -0.25 | 2.25 | **0.03** | **1.90** | 0.02 | 2.49 | -0.05 | 2.37 | -0.01 | 2.60 | -0.12 | 1.85 |

Table C.10: Spearman's correlation (ρ) and two sample KS test for U27 mode HV image.

| Texture measure | Coefficient of Variation | | Energy | | Kurtosis | | Mean | | Skewness | | Variance | |
|---|---|---|---|---|---|---|---|---|---|---|---|---|
| Filter size | ρ | K-S | ρ | K-S | ρ | K-S | ρ | K-S | ρ | K-S | ρ | K-S |
| 79 | -.437 | 1.548 | **.373** | **2.673** | -.335 | 1.700 | .437 | 2.720 | -.347 | 1.548 | .341 | 2.673 |
| 81 | -.437 | 1.442 | .364 | 2.566 | -.349 | 1.634 | .435 | 2.643 | -.366 | 1.442 | .340 | 2.625 |
| 83 | **-.449** | **1.640** | .365 | 2.610 | -.364 | 1.821 | .434 | 2.643 | **-.386** | **1.640** | .340 | 2.625 |
| 85 | -.444 | 1.519 | .362 | 2.610 | -.356 | 1.634 | **.435** | **2.643** | -.379 | 1.519 | .339 | 2.504 |
| 87 | -.442 | 1.670 | .363 | 2.598 | -.360 | 1.649 | .435 | 2.643 | -.378 | 1.670 | .338 | 2.474 |
| 89 | -.435 | 1.563 | .362 | 2.533 | -.364 | 1.756 | .433 | 2.595 | -.376 | 1.563 | .338 | 2.426 |
| 91 | -.416 | 1.655 | .359 | 2.477 | **-.367** | **1.777** | .426 | 2.595 | -.377 | 1.655 | .338 | 2.566 |

Table C.11: Spearman's correlation (ρ) and two sample KS test for U27 mode HH image.

| Texture measure | Coefficient of Variation | | Energy | | Kurtosis | | Mean | | Skewness | | Variance | |
|---|---|---|---|---|---|---|---|---|---|---|---|---|
| Filter size | ρ | K-S | ρ | K-S | ρ | K-S | ρ | K-S | ρ | K-S | ρ | K-S |
| 79 | -0.495 | 2.367 | **0.244** | **2.518** | -0.336 | 2.640 | 0.302 | 2.563 | -0.377 | 2.566 | **0.201** | **2.610** |
| 81 | -0.498 | 2.337 | 0.243 | 2.610 | -0.333 | 2.640 | 0.292 | 2.563 | -0.374 | 2.504 | 0.199 | 2.610 |
| 83 | **-0.502** | **2.260** | 0.239 | 2.518 | -0.329 | 2.640 | 0.297 | 2.563 | -0.367 | 2.563 | 0.195 | 2.489 |
| 85 | -0.492 | 2.260 | 0.237 | 2.504 | -0.326 | 2.563 | 0.297 | 2.625 | -0.367 | 2.563 | 0.199 | 2.489 |
| 87 | -0.495 | 2.260 | 0.236 | 2.456 | -0.326 | 2.563 | 0.298 | 2.625 | -0.368 | 2.563 | 0.198 | 2.536 |
| 89 | -0.493 | 2.260 | 0.241 | 2.489 | -0.320 | 2.563 | 0.296 | 2.625 | -0.371 | 2.563 | 0.203 | 2.459 |
| 91 | -0.492 | 2.260 | 0.236 | 2.489 | -0.317 | 2.640 | 0.299 | 2.625 | -0.374 | 2.563 | 0.199 | 2.459 |

Table C.12: Spearman's correlation (ρ) and two sample KS test for U17 mode VH image.

| Texture measure | Coefficient of Variation | | Energy | | Kurtosis | | Mean | | Skewness | | Variance | |
|---|---|---|---|---|---|---|---|---|---|---|---|---|
| Filter size | ρ | K-S | ρ | K-S | ρ | K-S | ρ | K-S | ρ | K-S | ρ | K-S |
| 79 | -0.42 | 2.19 | 0.33 | 2.61 | -0.46 | 2.28 | 0.35 | 2.55 | -0.43 | 2.00 | **0.31** | **2.61** |
| 81 | -0.42 | 2.17 | 0.32 | 2.61 | -0.45 | 2.17 | 0.35 | 2.55 | -0.42 | 2.09 | 0.30 | 2.61 |
| 83 | **-0.44** | **2.20** | **0.32** | **2.61** | -0.46 | 2.21 | 0.34 | 2.50 | -0.45 | 2.00 | 0.29 | 2.61 |
| 85 | -0.43 | 2.05 | 0.32 | 2.61 | **-0.47** | **2.17** | **0.35** | **2.55** | -0.45 | 2.00 | 0.29 | 2.61 |
| 87 | -0.43 | 1.99 | 0.32 | 2.50 | -0.49 | 2.17 | 0.35 | 2.55 | -0.46 | 1.94 | 0.29 | 2.61 |
| 89 | -0.43 | 1.99 | 0.31 | 2.50 | -0.48 | 2.17 | 0.34 | 2.55 | **-0.46** | **2.09** | 0.29 | 2.50 |
| 91 | -0.42 | 1.99 | 0.31 | 2.50 | -0.47 | 2.30 | 0.35 | 2.55 | -0.44 | 2.05 | 0.30 | 2.50 |

Table C.13: Spearman's correlation (ρ) and two sample KS test for SQ mode HH image.

| Filter size | Energy | | Mean | | Variance | |
|---|---|---|---|---|---|---|
| | ρ | K-S | ρ | K-S | ρ | K-S |
| 29 | .260 | 2.152 | **.180** | **2.260** | .135 | 1.833 |
| 31 | **.267** | **2.261** | .173 | 2.156 | .125 | 1.833 |
| 33 | .258 | 2.164 | .171 | 2.156 | .123 | 1.851 |
| 35 | .250 | 2.152 | .167 | 2.154 | **.445** | **2.097** |
| 37 | .248 | 2.152 | .168 | 2.154 | .440 | 2.097 |
| 39 | .243 | 2.140 | .156 | 2.168 | .433 | 2.032 |
| 41 | .226 | 2.092 | .149 | 2.290 | .431 | 1.990 |

Table C.14: Spearman's correlation (ρ) and two sample KS test for SQ mode HV image.

| Filter size | Energy | | Mean | | Variance | |
|---|---|---|---|---|---|---|
| | ρ | K-S | ρ | K-S | ρ | K-S |
| 29 | .456 | 2.326 | .443 | 2.326 | .444 | 2.219 |
| 31 | **.457** | **2.204** | **.447** | **2.219** | **.450** | **2.112** |
| 33 | .451 | 2.112 | .440 | 2.112 | .442 | 2.097 |
| 35 | .452 | 2.204 | .439 | 2.082 | .440 | 2.082 |
| 37 | .445 | 2.204 | .434 | 2.082 | .432 | 2.082 |
| 39 | .442 | 1.990 | .438 | 2.082 | .436 | 2.082 |
| 41 | .430 | 1.990 | .431 | 2.082 | .433 | 2.082 |

Table C.15: Spearman's correlation (ρ) and two sample KS test for SQ mode VH image.

| Filter size | Energy | | Mean | | Variance | |
|---|---|---|---|---|---|---|
| | ρ | K-S | ρ | K-S | ρ | K-S |
| 29 | 0.489 | 2.326 | 0.487 | 2.326 | 0.493 | 2.112 |
| 31 | **0.498** | **2.204** | **0.494** | **2.204** | 0.495 | 2.156 |
| 33 | 0.495 | 2.097 | 0.491 | 2.112 | 0.491 | 2.097 |
| 35 | 0.492 | 2.097 | 0.493 | 2.082 | 0.489 | 2.017 |
| 37 | 0.488 | 2.097 | 0.487 | 2.082 | 0.484 | 2.032 |
| 39 | 0.489 | 2.097 | 0.491 | 2.082 | 0.485 | 2.017 |
| 41 | 0.492 | 1.990 | 0.484 | 2.082 | **0.499** | **1.976** |

Table C.16: Spearman's correlation (ρ) and two sample KS test for SQ mode VV image.

| Filter size | Energy | | Mean | | Variance | |
|---|---|---|---|---|---|---|
| | ρ | K-S | ρ | K-S | ρ | K-S |
| 29 | .156 | 2.094 | .199 | 2.139 | .117 | 1.940 |
| 31 | .162 | 1.984 | **.196** | **2.245** | .127 | 1.863 |
| 33 | **.165** | **2.032** | .183 | 2.245 | **.128** | **1.848** |
| 35 | .150 | 1.970 | .179 | 2.062 | .127 | 1.863 |
| 37 | .156 | 2.032 | .185 | 2.168 | .116 | 1.878 |
| 39 | .141 | 2.047 | .175 | 2.168 | .116 | 1.925 |
| 41 | .124 | 2.183 | .154 | 2.168 | .098 | 2.047 |

Table C.17: Spearman's correlation (ρ) and two sample KS test for FQ mode HH image.

| Filter size | Energy | | Mean | | Variance | |
|---|---|---|---|---|---|---|
| | ρ | K-S | ρ | K-S | ρ | K-S |
| 29 | **-.213** | **1.126** | **-.152** | **1.429** | -.243 | 1.002 |
| 31 | -.185 | 1.093 | -.122 | 1.093 | -.221 | .969 |
| 33 | -.201 | 1.057 | -.121 | 1.093 | -.235 | .721 |
| 35 | -.190 | 1.057 | -.129 | 1.163 | -.233 | .881 |
| 37 | -.187 | 1.057 | -.127 | 1.163 | -.241 | .812 |
| 39 | -.198 | .987 | -.116 | 1.075 | -.198 | .987 |
| 41 | -.208 | .812 | -.145 | .848 | **-.243** | **.812** |

Table C.18: Spearman's correlation (ρ) and two sample KS test for FQ mode HV image.

| Filter size | Energy | | Mean | | Variance | |
|---|---|---|---|---|---|---|
| | ρ | K-S | ρ | K-S | ρ | K-S |
| 29 | .544 | 1.974 | .566 | 1.941 | .504 | 2.029 |
| 31 | .556 | 1.747 | .581 | 1.883 | .520 | 1.675 |
| 33 | **.581** | **1.835** | .599 | 1.711 | .558 | 1.817 |
| 35 | -.129 | 1.163 | **.606** | **1.871** | **.559** | **1.871** |
| 37 | -.127 | 1.163 | .602 | 1.759 | .534 | 1.765 |
| 39 | -.116 | 1.075 | .599 | 1.529 | .537 | 1.553 |
| 41 | -.145 | .848 | .599 | 1.759 | .543 | 1.341 |

Table C.19: Spearman's correlation (ρ) and two sample KS test for FQ mode VH image.

| Filter size | Energy | | Mean | | Variance | |
|---|---|---|---|---|---|---|
| | ρ | K-S | ρ | K-S | ρ | K-S |
| 29 | .667 | 2.701 | .720 | 2.719 | .588 | 2.522 |
| 31 | .689 | 2.737 | .741 | 2.701 | **.619** | **2.701** |
| 33 | .689 | 2.665 | .738 | 2.665 | .600 | 2.365 |
| 35 | **.690** | **2.541** | **.748** | **2.559** | .599 | 2.453 |
| 37 | .662 | 2.332 | .734 | 2.559 | .593 | 2.171 |
| 39 | .633 | 2.489 | .730 | 2.683 | .557 | 2.489 |
| 41 | .639 | 2.489 | .710 | 2.701 | .567 | 2.383 |

Table C.20: Spearman's correlation (ρ) and two sample KS test for FQ mode HV image.

| Filter size | Energy | | Mean | | Variance | |
|---|---|---|---|---|---|---|
| | ρ | K-S | ρ | K-S | ρ | K-S |
| 29 | .448 | 1.851 | .483 | 1.913 | 0.419 | 1.729 |
| 31 | .444 | 1.729 | .492 | 1.851 | .419 | 1.729 |
| 33 | .441 | 1.637 | .500 | 1.715 | .420 | 1.623 |
| 35 | .460 | 1.620 | .492 | 1.821 | .420 | 1.741 |
| 37 | .460 | 1.528 | .503 | 1.715 | .424 | 1.528 |
| 39 | .451 | 1.495 | **.510** | **1.593** | .413 | 1.332 |
| 41 | **.466** | **1.495** | .510 | 1.560 | **.441** | **1.495** |